Systematic investigation of nuclear incompressibility and finite-range exchange effects in density-dependent *NN* interactions on *α*-decay half-lives

M. M. Mesmh M. Ismail A. Adel† A. R. Abdulghany

Physics Department, Faculty of Science, Cairo University, Giza 12613, Egypt

Abstract: We present a systematic investigation of α-decay half-lives for nuclei with $52 \le Z \le 122$ within a microscopic double-folding framework. The α–nucleus potentials are constructed from the Michigan three-range Yukawa (M3Y) nucleon–nucleon interaction and its density-dependent variants (DDM3Y, CDM3Y, and BDM3Y), explicitly incorporating both direct and exchange terms. Special emphasis is placed on the role of finite-range exchange effects, which provide a more realistic description than the conventional zero-range approximation and lead to noticeable modifications in the Coulomb barrier region. Barrier penetrabilities are calculated using the WKB approximation with the Bohr–Sommerfeld quantization condition. The results demonstrate that nuclear deformation generally enhances the tunneling probability, resulting in shorter α-decay half-lives. Furthermore, the calculations indicate that increasing the nuclear incompressibility parameter K within the CDM3Y family tends to shorten the predicted half-lives by slightly enhancing the barrier penetrability. The calculated isotopic trends reflect the characteristic behavior near the neutron shell closures at $N = 82$, 126, and 184, highlighting the interplay between nuclear structure effects and decay dynamics. Overall, the results provide a systematic assessment of the sensitivity of α-decay half-lives to finite-range exchange, density dependence, deformation, and nuclear incompressibility within this microscopic double-folding approach.

Keywords: nuclear incompressibility, α-decay, finite-range exchange, density-dependen *NN* interactions, Superheavy nuclei

DOI: 10.1088/1674-1137/ae904e **CSTR:** 32044.14.ChinesePhysicsC.50114103

I. INTRODUCTION

Alpha decay constitutes one of the primary decay modes of heavy and superheavy nuclei (SHN) and provides a sensitive probe of their underlying nuclear structure properties [1−9]. From an experimental perspective, the discovery and identification of superheavy elements (SHEs) rely predominantly on the observation of characteristic α-decay chains, which play a decisive role in extending the nuclear chart toward the region of the heaviest nuclei [10−15]. A representative example is the synthesis of the even–even isotope $^{294}_{118}$Og through the hot-fusion reaction ^{48}Ca + ^{249}Cf at JINR Dubna [16]. This nucleus, with a measured half-life of $0.89^{+1.07}_{-0.31}$ ms, undergoes a cascade of successive α decays that ultimately terminates in spontaneous fission [16]. Subsequent experiments employing mixed-Cf targets irradiated with a ^{48}Ca beam have revealed additional α-decay chains, suggesting the possible existence of neighboring isotopes such as ^{295,296}Og [17]. Combined with theoretical analyses, these observations provide valuable insights into the enhanced stability of SHN and the role of underlying shell effects [2, 7, 14, 15, 18].

From a theoretical standpoint, a quantitative microscopic description of α-decay half-lives requires an accurate determination of the α–daughter nucleus interaction in the vicinity of the Coulomb barrier, where quantum tunneling governs the decay process [19−23]. In this context, the nucleus–nucleus potential constructed within the double-folding model plays a central role, as it directly controls the barrier penetrability and, consequently, the decay probability. A defining characteristic of this model is its intrinsic nonlocal nature, which arises from the fermionic character of nucleons and the reduction of the underlying many-body quantum problem to an effective two-body α–core system. Accurate treatment of nonlocality is therefore essential for reliable microscopic α-decay calculations [24−26].

In particular, Pauli nonlocality originates from the antisymmetrization of the total wave function of the emit-

Received 25 April 2026; Accepted 24 July 2026; Accepted manuscript online 25 July 2026

† E-mail: ahmedadel@sci.cu.edu.eg

©2026 Chinese Physical Society and the Institute of High Energy Physics of the Chinese Academy of Sciences and the Institute of Modern Physics of the Chinese Academy of Sciences and IOP Publishing Ltd. All rights, including for text and data mining, AI training, and similar technologies, are reserved.

ted α particle and the daughter nucleus, yielding exchange contributions in the effective interaction. These exchange effects are closely related to the knock-on exchange mechanism known from nucleon–nucleus scattering and are commonly incorporated in α-decay studies through the finite-range exchange component of the effective nucleon–nucleon (NN) interaction [2, 27−32]. Earlier studies by Rojas-Gamboa *et al.* demonstrated that the inclusion of such nonlocal exchange effects can significantly reduce both α- and cluster-decay half-lives [26]. Importantly, the magnitude of this reduction was shown to depend sensitively on the specific NN interaction adopted in the folding procedure, underscoring the need for realistic interaction inputs for a quantitative description of decay systematics.

A central ingredient of density-dependent effective interactions is the nuclear matter incompressibility coefficient, which characterizes the curvature of the nuclear matter equation of state (EOS) at saturation density [33]. Nuclear incompressibility plays a fundamental role in both nuclear structure and astrophysics, influencing the ground-state properties of finite nuclei, the stability of neutron-rich systems, the excitation energies of isoscalar giant monopole resonances (ISGMR), heavy-ion reaction dynamics, neutron-star structure, and core-collapse supernova simulations [34−36]. In finite nuclei, this coefficient is closely related to the surface energy and surface diffuseness, particularly in the transition region where the density deviates from its bulk value [37].

Although the nuclear matter incompressibility coefficient cannot be measured directly, it can be extracted from experimental ISGMR energies in medium and heavy nuclei, because the ISGMR represents a collective compression mode of nuclear matter [38]. Semiempirical macroscopic analyses and fully microscopic calculations employing various effective interactions have been used to constrain the nuclear matter incompressibility coefficient from available data.

Earlier studies have indicated that α-decay observables can provide useful information on the density dependence of the effective interaction and, consequently, on nuclear incompressibility. Seif [37] employed α decay to probe nuclear incompressibility by modifying the density-dependent M3Y interaction in the strong-overlap region and extracting incompressibility values from experimental half-lives. More recently, systematic studies of α-decay preformation factors using different microscopic M3Y-, DDM3Y-, CDM3Y-, and BDM3Y-based folding potentials have shown that the choice of effective interaction affects the inner turning point, barrier profile, penetrability, and extracted preformation probabilities [39]. These works collectively demonstrate that α-decay observables are governed not only by the decay energy and Coulomb barrier, but also by the density-dependent nuclear interaction that shapes the microscopic α–daughter potential.

This established relation underscores that the density dependence of the effective NN interaction is closely linked to the nuclear equation of state (EOS) and the incompressibility. Once the functional form of the density-dependent term is specified, the EOS and the corresponding incompressibility can be determined [40]. Consequently, these quantities cannot be chosen independently. The sensitivity of nucleus–nucleus potentials to incompressibility is particularly significant in the region of strong density overlap, where nuclear saturation properties dominate. For this reason, refractive elastic and quasielastic scattering of α particles and strongly bound light nuclei over broad energy ranges have been extensively analyzed as indirect probes of the density dependence of the effective NN force and, hence, of the nuclear EOS [33, 41]. In α decay, a nearly complete overlap occurs between the compact, high-density α particle and the daughter nucleus immediately prior to barrier penetration, while both remain essentially in their ground states [37]. This configuration provides a sensitive testing ground for the density dependence of the effective interaction over a wide density interval. By constructing the α–daughter potential using density-dependent NN forces within the double-folding model and evaluating the barrier penetrability through the WKB approximation, a direct assessment of the impact of nuclear incompressibility and medium effects on calculated half-lives is possible. The extensive body of experimental α-decay data thus offers a valuable opportunity to constrain interaction properties and nuclear matter parameters through decay observables.

Among the finite-range interactions, the Michigan three-range Yukawa (M3Y) interaction has been widely employed in folding calculations of heavy-ion optical potentials [41, 42]. Originally constructed by fitting G-matrix elements based on realistic Reid and Paris NN interactions, the M3Y potential was designed to reproduce both the long-range one-pion-exchange tail and the short-range repulsive core associated with heavier-meson exchange. However, the original density-independent M3Y interaction fails to reproduce the empirical saturation properties of cold nuclear matter [41]. This limitation can be overcome by introducing an explicit density dependence into the interaction, thereby effectively incorporating medium effects and nuclear incompressibility.

Alongside these developments, various microscopic and semiempirical approaches have been proposed to describe α-decay half-lives. Such microscopic models include the generalized liquid drop model (GLDM) [43, 44], the density-dependent cluster model (DDCM) [21, 45, 46], the unified fission model (UFM) [7], the Coulomb and proximity potential model (CPPM) [47−49], and the two-potential approach (TPA) [50, 51], among others. In parallel, numerous empirical and semiempirical formulas—largely based on the α-decay energy Q_α—

have been developed and continuously refined as new experimental data become available [3, 52–55]. Despite their overall success, the extent to which α-decay half-lives depend on key ingredients of the effective interaction, particularly nuclear incompressibility and finite-range exchange effects, remains an open and timely question.

Motivated by these considerations, the present work investigates the sensitivity of α-decay half-lives of heavy and superheavy nuclei to nuclear incompressibility and finite-range exchange effects of density-dependent NN interactions within the double-folding framework. Special emphasis is placed on assessing how these interaction components influence the α–nucleus potential in the vicinity of the Coulomb barrier and, consequently, the predicted decay probabilities.

The paper is organized as follows. Section II presents the theoretical formalism, including the construction of the Coulomb and nuclear potentials within the adopted microscopic framework, explicitly including nuclear deformation, finite-range exchange effects, and density-dependent nucleon–nucleon interactions. It also describes the evaluation of the assault frequency, barrier penetrability, preformation factor, and decay width. Section III presents the analysis and discussion of the calculated α-decay half-lives, while Sec. IV summarizes the main results and concludes the paper.

II. THEORETICAL FRAMEWORK

A. The deformed density-dependent cluster model

Within the density-dependent cluster model, incorporating the effects of nuclear deformation, the α particle is assumed to interact with an axially symmetric deformed daughter nucleus. The total interaction potential between the emitted α particle and the daughter nucleus is expressed as the sum of the nuclear, Coulomb, and centrifugal contributions, and is given by [22, 45, 56]

$$V_{\rm T}(R,\theta) = \lambda(\theta)\, V_N(R,\theta) + V_C(R,\theta) + \frac{\hbar^2}{2\mu}\frac{\left(\ell+\frac{1}{2}\right)^2}{R^2}, \qquad (1)$$

where θ denotes the orientation angle of the deformed daughter nucleus, and $\lambda(\theta)$ is a renormalization factor for the nuclear interaction. The variable R represents the distance between the centers of mass of the α particle and the daughter nucleus, and ℓ is the orbital angular momentum carried by the α particle. The Langer modification [24, 57], $\ell(\ell+1) \to (\ell+1/2)^2$, is adopted to ensure the validity of the first-order WKB approximation [24]. The parameter μ denotes the reduced mass of the α–daughter system.

The allowed values of the angular momentum ℓ are determined by the spin–parity selection rules

$$|J_i - J_f| \le \ell \le J_i + J_f \quad \text{and} \quad \frac{\pi_f}{\pi_i} = (-1)^\ell, \qquad (2)$$

where J_i and J_f are the spins of the parent and daughter nuclei, respectively, and π_i and π_f denote their parities. For each decay, the minimum value of ℓ that satisfies both conditions in Eq. (2) is adopted and denoted by $\ell_{\rm min}$. When the spin and parity assignments of these nuclei are not experimentally known, the angular momentum transfer is assumed to be $\ell_{\rm min} = 0$.

Within the double-folding formalism, the nuclear and Coulomb interaction potentials for a spherical-deformed system are calculated as [22, 56]

$$V_{N(C)}(R,\theta) = \int {\rm d}\boldsymbol{r}_1 \int {\rm d}\boldsymbol{r}_2 \rho_\alpha(\boldsymbol{r}_1)\, \upsilon_{N(C)}(s)\, \rho_d(\boldsymbol{r}_2), \qquad (3)$$

where $\boldsymbol{s} = \boldsymbol{r}_2 - \boldsymbol{r}_1 + \boldsymbol{R}$ is the relative separation between the interacting nucleons. The term $\upsilon_C(s)$ represents the standard proton–proton interaction, $\upsilon_C(s) = e^2/s$. The effective nucleon–nucleon interaction, $\upsilon_N(s)$, is described by the M3Y-Paris potential [42].

The explicit form of the M3Y-Paris interaction is given by

$$\upsilon_N(s) = \left[11061.625\,\frac{e^{-4s}}{4s} - 2537.5\,\frac{e^{-2.5s}}{2.5s}\right] - 590\left[1 - 0.002\left(\frac{E_\alpha}{A_\alpha}\right)\right]\delta(\boldsymbol{s}), \qquad (4)$$

where E_α and A_α denote the kinetic energy and mass number of the α particle, respectively. The zero-range delta-function term approximates the knock-on exchange contribution. A more realistic description can be obtained using a finite-range exchange interaction; however, this treatment requires a self-consistent determination of the interaction potential.

The matter density distribution of the α particle is assumed to follow a Gaussian form, given by

$$\rho_\alpha(r_1) = 0.4229\exp\left(-0.7024\, r_1^2\right). \qquad (5)$$

The matter or charge density of the deformed daughter nucleus is described by a two-parameter Fermi distribution,

$$\rho(r,\theta') = \frac{\rho_0}{1+\exp\left(\frac{r-R(\theta')}{a}\right)}, \qquad (6)$$

where the normalization constant ρ_0 is determined by requiring that the integral of the density yields the corresponding mass number or proton number for the matter

and charge densities, respectively. Here, θ' denotes the angle between the position vector $\boldsymbol{r}$ and the symmetry axis of the deformed nucleus. The orientation-dependent half-density radius $R(\theta')$ is expressed as

$$R(\theta') = R_0\left[1+\beta_2 Y_{2,0}(\theta')+\beta_4 Y_{4,0}(\theta')+\beta_6 Y_{6,0}(\theta')\right], \quad (7)$$

where β_2, β_4, and β_6 represent the quadrupole, hexadecapole, and hexacontatetrapole deformation parameters, respectively, obtained from the WS4 mass model [58]. The radius parameter R_0 and the diffuseness a are adopted from Refs. [21, 22] and given by

$$R_0 = 1.07A_d^{1/3}\ \text{fm}, \qquad a = 0.54\ \text{fm}. \quad (8)$$

The renormalization factor λ in the nuclear potential [Eq. (1)] is determined using the Bohr–Sommerfeld quantization condition [59],

$$\int_{R_1(\theta)}^{R_2(\theta)} \mathrm{d}r\, k(r,\theta) = (2n+1)\frac{\pi}{2} = (G-\ell+1)\frac{\pi}{2}, \quad (9)$$

where the local wave number is defined as

$$k(r,\theta) = \sqrt{\frac{2\mu}{\hbar^2}|V_T(r,\theta)-Q_\alpha|}. \quad (10)$$

The global quantum number G is set to $G=20$ for $N>126$ and $G=18$ for $82<N\le 126$ [21, 46]. When available, the α-decay energy, Q_α, is taken from the AME2020 experimental mass evaluation [60]. For superheavy nuclei lacking experimental mass or Q_α data, these values are adopted from the WS4+ mass table [58]. WS4+ denotes the Weizsäcker–Skyrme (WS) macroscopic–microscopic mass model supplemented by the radial basis function (RBF) correction [58, 61]. This mass model is particularly appropriate for superheavy nuclei, as WS4+ provides a highly accurate description of α-decay Q values in this region [58]. The quantities R_i $(i=1,2,3)$ denote the classical turning points of the α–daughter interaction potential, determined by the condition $V_T(r,\theta)|_{r=R_i} = Q_\alpha$.

For a given emission angle θ, the assault frequency and barrier penetrability within the WKB approximation are expressed as

$$\nu(\theta) = \left[\int_{R_1(\theta)}^{R_2(\theta)} \frac{2\mu}{\hbar k(r,\theta)}\mathrm{d}r\right]^{-1}, \quad (11)$$

$$P(\theta) = \exp\left[-2\int_{R_2(\theta)}^{R_3(\theta)} k(r,\theta)\,\mathrm{d}r\right]. \quad (12)$$

The partial α-decay width corresponding to the emission angle θ is then given by

$$\Gamma(\theta) = \hbar S_\alpha \nu(\theta) P(\theta), \quad (13)$$

where S_α denotes the α-particle preformation probability. In the present work, this probability is evaluated using the analytical expression proposed by Deng *et al.* [62]. This expression provides a refined and comprehensive approach to estimating the α-preformation factor in both favored and unfavored α-decay transitions. The preformation probability S_α is calculated as

$$\log_{10}S_\alpha = a + bA_p^{1/6}\sqrt{Z_p} + c\frac{Z_p}{\sqrt{Q_\alpha}} - d\chi' - e\rho' + f\sqrt{\ell(\ell+1)}, \quad (14)$$

where the first three terms are derived from the well-known semi-empirical Royer relation [55, 63, 64], and the fourth and fifth terms are based on the universal decay law (UDL) proposed by Qi *et al.* [65]. Within this framework, the quantities χ' and ρ' are defined as

$$\chi' = Z_\alpha Z_d\sqrt{\frac{A_\alpha A_d}{(A_\alpha+A_d)Q_\alpha}}, \quad (15)$$

$$\rho' = \sqrt{\frac{A_\alpha A_d}{A_\alpha+A_d}Z_\alpha Z_d\left(A_\alpha^{1/3}+A_d^{1/3}\right)}. \quad (16)$$

The last term in Eq. (14) explicitly incorporates the angular momentum ℓ carried by the emitted α particle, thereby accounting for the hindrance effect associated with the centrifugal barrier. This feature enables a unified description of both favored and unfavored decay modes. The adjustable parameters a, b, c, d, e, and f are taken from Ref. [62], where they were optimized to reproduce experimental data across a wide range of nuclei. Consequently, this expression provides a reliable estimate of the α-particle preformation probability and enhances the predictive capability of α-decay half-life calculations. Moreover, it offers valuable insight into the underlying microscopic nuclear-structure effects, such as shell closures and angular-momentum hindrance, that significantly influence the α-decay process.

The total decay width is obtained by averaging over all possible orientations of the daughter nucleus,

$$\Gamma = \frac{1}{2}\int_0^\pi \Gamma(\theta)\sin\theta\,\mathrm{d}\theta. \quad (17)$$

Finally, the α-decay half-life is related to the total decay width by

$$T_{1/2} = \frac{\hbar \ln 2}{\Gamma}. \tag{18}$$

B. Zero-range exchange *NN* interaction

Most calculations of α-decay and cluster-decay half-lives within the density-dependent cluster model employ the zero-range approximation for the exchange component of the effective nucleon–nucleon interaction. In this approximation, the knock-on exchange contribution is represented by a delta-function interaction,

$$v_{\rm Ex}(\boldsymbol{s}) = -590\,(1 - 0.002E_\alpha/A_\alpha)\,\delta(\boldsymbol{s}), \tag{19}$$

where $\boldsymbol{s} = \boldsymbol{r}_2 - \boldsymbol{r}_1 + \boldsymbol{R}$ is the separation vector between the interacting nucleons. The delta function significantly simplifies the double-folding calculation because the exchange term becomes local and can be added directly to the direct term.

Using the Fourier transform representation, the nuclear part of the folded potential can be written as

$$V_N(\boldsymbol{R}) = \int \mathrm{d}\boldsymbol{k}\, \mathrm{e}^{\mathrm{i}\boldsymbol{k}\cdot\boldsymbol{R}} \tilde{v}_N(k) \int \mathrm{d}\boldsymbol{r}_1\, \mathrm{e}^{-\mathrm{i}\boldsymbol{k}\cdot\boldsymbol{r}_1} \rho_\alpha(r_1) \times \int \mathrm{d}\boldsymbol{r}_2\, \mathrm{e}^{\mathrm{i}\boldsymbol{k}\cdot\boldsymbol{r}_2} \rho_d(r_2). \tag{20}$$

where $\tilde{v}_N(k)$ is the Fourier transform of the effective interaction, which includes both the direct M3Y-Paris terms and the zero-range exchange term,

$$\tilde{v}_N(k) = 4\pi \left[\frac{11061.6}{4(k^2+16)} - \frac{2537.5}{2.5(k^2+6.25)} \right] - 590\,(1 - 0.002E_\alpha/A_\alpha). \tag{21}$$

This zero-range formulation is employed for the ZR calculations discussed in Sec. III, whereas the finite-range exchange treatment is presented in the following subsection. The zero-range exchange approximation yields a computationally efficient form of the double-folding potential by reducing the exchange contribution to a local term that can be added directly to the direct part of the M3Y interaction. The integrals in the Fourier-transform representation were evaluated numerically using the standard procedures described in Refs. [22, 42, 66].

C. Density-dependent M3Y *NN* interaction

It is well established that the original density-independent M3Y effective nucleon–nucleon (NN) interaction fails to reproduce the empirical saturation properties of cold nuclear matter. This shortcoming is addressed by introducing an explicit density dependence into the interaction, thereby accounting for medium effects and nuclear incompressibility in a phenomenological yet physically motivated manner. Consequently, the density-dependent M3Y interaction is adopted in the present work to provide a more realistic description of the nuclear potential.

Within this framework, the effective NN interaction is assumed to take a separable form, where the density dependence is factored out of the radial part and expressed as

$$v_{D(EX)}(\rho, E, s) = F(\rho)\, g(E)\, v_{D(EX)}(s), \tag{22}$$

where v_D and v_{EX} denote the direct and exchange components of the interaction, respectively, derived from the M3Y interaction; s is the internucleon separation; and ρ represents the density of the surrounding nuclear medium. Here, E is the incident (laboratory) energy per nucleon.

In the present folding calculations, the realistic M3Y–Paris effective nucleon–nucleon (NN) interaction is employed. The radial dependence of this interaction is expressed as a superposition of three Yukawa functions, providing a physically motivated finite-range description. The interaction consists of direct and exchange components, whose explicit forms are presented below. The direct component of the M3Y–Paris interaction is written as

$$v_D(s) = 11061.625\,\frac{e^{-4s}}{4s} - 2537.5\,\frac{e^{-2.5s}}{2.5s}, \tag{23}$$

while the finite-range exchange component takes the form

$$v_{\rm Ex}(s) = -1524.25\,\frac{e^{-4s}}{4s} - 518.75\,\frac{e^{-2.5s}}{2.5s} - 7.8474\,\frac{e^{-0.7072s}}{0.7072s}. \tag{24}$$

The explicit form of the density-dependent factor $F(\rho)$ is given by

$$F(\rho) = C\left[1 + \alpha \exp(-\beta\rho) - \gamma\rho\right], \tag{25}$$

where the parameters C, α, β, and γ (Table 1) are adjusted to reproduce the empirical binding energy of cold nuclear matter, $E/A = -16$ MeV, at the saturation density $\rho_0 = 0.17$ fm^{-3}. The overlap density entering the density-dependent factor $F(\rho)$ is typically taken as the sum of the projectile and target densities.

The energy-dependent factor in Eq. (22) is assumed to vary linearly with the incident energy per nucleon E. For the M3Y–Paris interaction, this factor is expressed as

Table 1. The parameters corresponding to the different density-dependent forms of $F(\rho)$ employed in the M3Y–Paris interaction are listed, along with the nuclear incompressibility values, K.

Interaction	C	α	β/fm^3	γ/fm^3	K/MeV
DDM3Y1	0.2963	3.7231	3.7384	0.0	176
CDM3Y1	0.3429	3.0232	3.5512	0.5	188
CDM3Y2	0.3346	3.0357	3.0685	1.0	204
CDM3Y3	0.2985	3.4528	2.6388	1.5	217
CDM3Y4	0.3052	3.2998	2.3180	2.0	228
CDM3Y5	0.2728	3.7367	1.8294	3.0	241
CDM3Y6	0.2658	3.8033	1.4099	4.0	252
BDM3Y1	1.2521	0.0	0.0	1.7452	270

$$g(E) = 1 - 0.003\,E/A. \tag{26}$$

This phenomenological dependence was introduced [27, 33, 41] to incorporate the explicit, albeit weak, energy dependence of the effective nucleon–nucleon interaction, which is necessary to reproduce the empirical energy dependence of the nucleon optical potential.

D. Effect of finite-range exchange *NN* interaction

The nonlocality arising from the Pauli exclusion principle stems from exchange effects that require proper antisymmetrization between the nucleons of the emitted α particle and those of the daughter nucleus [25]. In many earlier α-decay studies, the exchange component of the nucleon–nucleon (NN) interaction has been treated using the zero-range approximation [21], effectively neglecting explicit antisymmetrization effects. For systems where both the α particle and the daughter nucleus exhibit spherical symmetry, the dominant contribution from nucleon exchange can be naturally incorporated into the folding model by employing a finite-range exchange interaction [27].

Within this framework, the direct and exchange components of the nuclear interaction potential are expressed as [27]

$$V_D(R) = \int \mathrm{d}\boldsymbol{r}_1 \int \mathrm{d}\boldsymbol{r}_2 \rho_\alpha(\boldsymbol{r}_1)\upsilon_D(E,s)\rho_d(\boldsymbol{r}_2), \tag{27}$$

and

$$V_{\rm Ex}(R) = \int \mathrm{d}\boldsymbol{r}_1 \int \mathrm{d}\boldsymbol{r}_2 \rho_\alpha(\boldsymbol{r}_1,\boldsymbol{r}_1+\boldsymbol{s})\rho_d(\boldsymbol{r}_2,\boldsymbol{r}_2-\boldsymbol{s}) \times \upsilon_{\rm Ex}(E,s)\exp\left[\frac{\mathrm{i}\,\boldsymbol{k}(R)\cdot\boldsymbol{s}}{M}\right], \tag{28}$$

where $\rho_{\alpha(d)}(\boldsymbol{r},\boldsymbol{r}')$ denote the one-body density matrices of the α particle and the daughter nucleus, respectively, and $M = A_\alpha A_d/(A_\alpha + A_d)$, where $A_\alpha = 4$ and A_d are the mass numbers of the emitted α particle and the daughter nucleus, respectively.

The local relative-motion momentum $k(R)$ is defined as [27]

$$k^2(R) = \frac{2\mu}{\hbar^2}\left[E_{\rm c.m.} - V_N(R) - V_C(R)\right], \tag{29}$$

where $E_{\rm c.m.}$ is the center-of-mass energy. The total nuclear potential is given by $V_N(R) = V_D(R) + V_{\rm Ex}(R)$, and $V_C(R)$ denotes the Coulomb interaction.

Owing to the exchange term, the folded nuclear potential becomes nonlocal and energy-dependent, leading to a self-consistency problem because the momentum $k(R)$ itself depends on $V_N(R)$. This issue is resolved numerically using a rapidly converging iterative procedure.

An exact treatment of the nonlocal exchange potential is computationally demanding. Consequently, an equivalent local potential is obtained by applying a realistic localization of the density matrix [67, 68]. In this approximation, the nonlocal densities are expressed as [68]

$$\rho(\boldsymbol{r},\boldsymbol{r}+\boldsymbol{s}) \simeq \rho\left(\boldsymbol{r}+\frac{\boldsymbol{s}}{2}\right)\hat{j}_1\left[k_{\rm eff}\left(\boldsymbol{r}+\frac{\boldsymbol{s}}{2}\right)s\right], \tag{30}$$

where

$$\hat{j}_1(x) = \frac{3\,j_1(x)}{x} = \frac{3(\sin x - x\cos x)}{x^3}. \tag{31}$$

The α particle represents a special case in which the ground-state density can be accurately described by a simple Gaussian distribution. Assuming that the four nucleons of ^{4}He occupy the lowest $s_{1/2}$ harmonic-oscillator shell, the corresponding off-diagonal one-body density matrix can be written as [27, 69]

$$\rho_\alpha(\boldsymbol{r},\boldsymbol{r}+\boldsymbol{s}) \simeq \rho_\alpha\left(\left|\boldsymbol{r}+\frac{\boldsymbol{s}}{2}\right|\right)\exp\left(-\frac{s^2}{4b_\alpha^2}\right), \tag{32}$$

where b_α is the harmonic-oscillator parameter. In the present calculations, we adopt $b_\alpha = 1.1932$ fm. Using this value, the diagonal density reduces to [27],

$$\begin{aligned}\rho_\alpha(r) \equiv \rho_\alpha(r,r) &= \frac{4}{\pi^{3/2}b_\alpha^3}\exp\left(-\frac{r^2}{b_\alpha^2}\right)\\ &= 0.4229\exp(-0.7024r^2),\end{aligned} \tag{33}$$

which is identical to the Gaussian density employed in Eq. (5). Consequently, this α-particle density is consistently applied in both the zero-range and finite-range exchange calculations.

The effective local Fermi momentum $k_{\rm eff}(r)$ is given by [27]

$$k_{\rm eff}(r) = \left\{\frac{5}{3\rho(r)}\left[\tau(r) - \frac{1}{4}\nabla^2\rho(r)\right]\right\}^{1/2}, \tag{34}$$

where the kinetic energy density $\tau(r)$ is expressed as

$$\tau(r) = \frac{3}{5}\left(\frac{3\pi^2}{2}\right)^{2/3}\rho(r)^{5/3} + \frac{1}{3}\nabla^2\rho(r) + \frac{1}{36}\frac{|\nabla\rho(r)|^2}{\rho(r)}. \tag{35}$$

The exchange component of the nucleus–nucleus interaction is expressed within the finite-range double-folding framework as [27, 32, 70]

$$\begin{aligned}V_{\rm Ex}(R) = 4\pi C\, g(E)&\int_0^\infty {\rm d}s\, s^2\, \upsilon_{\rm Ex}(E,s)\, j_0\left(\frac{k(R)s}{M}\right)\\ &\times\int {\rm d}\boldsymbol{y}\,\rho_d(|\boldsymbol{y}-\boldsymbol{R}|)\,\hat{j}_1\left(k_{\rm eff}^d(|\boldsymbol{y}-\boldsymbol{R}|)\,s\right)\\ &\times\rho_\alpha(y)\exp\left(-\frac{s^2}{4b_\alpha^2}\right)\\ &\times\left\{1+\alpha\exp\left[-\beta\left(\rho_\alpha(y)+\rho_d(|\boldsymbol{y}-\boldsymbol{R}|)\right)\right]\right.\\ &\left.-\gamma\left[\rho_\alpha(y)+\rho_d(|\boldsymbol{y}-\boldsymbol{R}|)\right]\right\}.\end{aligned} \tag{36}$$

The exchange potential in Eq. (36) is evaluated iteratively until self-consistency is achieved.

III. RESULTS AND DISCUSSION

The α-decay half-lives of nuclei in the atomic-number range $52 \le Z \le 122$ are systematically studied within a microscopic double-folding framework employing the effective Michigan three-range Yukawa (M3Y) nucleon–nucleon (NN) interaction and its density-dependent extensions, namely DDM3Y, CDM3Y, and BDM3Y. Particular attention is devoted to examining the sensitivity of the calculated α-decay half-lives of heavy and superheavy nuclei to nuclear incompressibility and to the finite-range exchange components inherent in the density-dependent NN interactions. These interaction properties significantly influence the structure of the microscopic α–nucleus potential, especially in the vicinity of the Coulomb barrier where the tunneling process occurs. Consequently, variations in the interaction parameters can lead to noticeable modifications in the barrier characteristics and, therefore, in the predicted decay probabilities.

In the notation used below, ZR-Sph denotes the density-independent M3Y–Paris interaction with the zero-range exchange approximation for a spherical daughter nucleus, whereas FR-Sph denotes the corresponding density-independent M3Y–Paris calculation with finite-range exchange. The density-dependent interactions DDM3Y, CDM3Y, and BDM3Y are implemented using finite-range exchange, consistent with the finite-range folding framework in which these parametrizations were originally constructed.

Before discussing the calculated potentials shown in Fig. 1, we briefly summarize the numerical treatment of the double-folding integrals. The direct nuclear and Coulomb terms, as well as the zero-range exchange contribution, involve only diagonal density distributions and were evaluated using the Fourier-transform representation of the folding potential [42]. The corresponding density form factors and density-dependent auxiliary functions, which are independent of the separation distance R, were calculated once and stored on a numerical mesh, following the standard procedure used in double-folding calculations [22]. For deformed daughter nuclei, the density was expanded in multipoles, such that the orientation dependence enters through the angular functions while the radial form factors are reused. In the finite-range exchange calculation, the exchange term contains non-diagonal density matrices and depends on the local relative-motion momentum $k(R)$; therefore, it was evaluated iteratively by updating $k(R)$ and the exchange potential until self-consistency was achieved. This numerical treatment follows the finite-range folding procedures described in Refs. [27, 29, 32].

Figure 1 displays the total α–nucleus interaction potential $V_T(R)$ as a function of the separation distance R for the α decay of ^{228}Rn $\rightarrow$ ^{224}Po $+\alpha$, calculated using several M3Y-based effective nucleon–nucleon interactions. The total potential consists of the microscopic double-folded nuclear interaction together with the Coulomb and centrifugal contributions. Different treatments of density dependence and exchange effects are evaluated using the FR-Sph, ZR-Sph, DDM3Y, CDM3Y, and BDM3Y interactions. As shown in Fig. 1(a), the calculated potentials exhibit the typical structure comprising a deep nuclear pocket at small separation distances followed by a repulsive Coulomb barrier at larger R. Although the overall

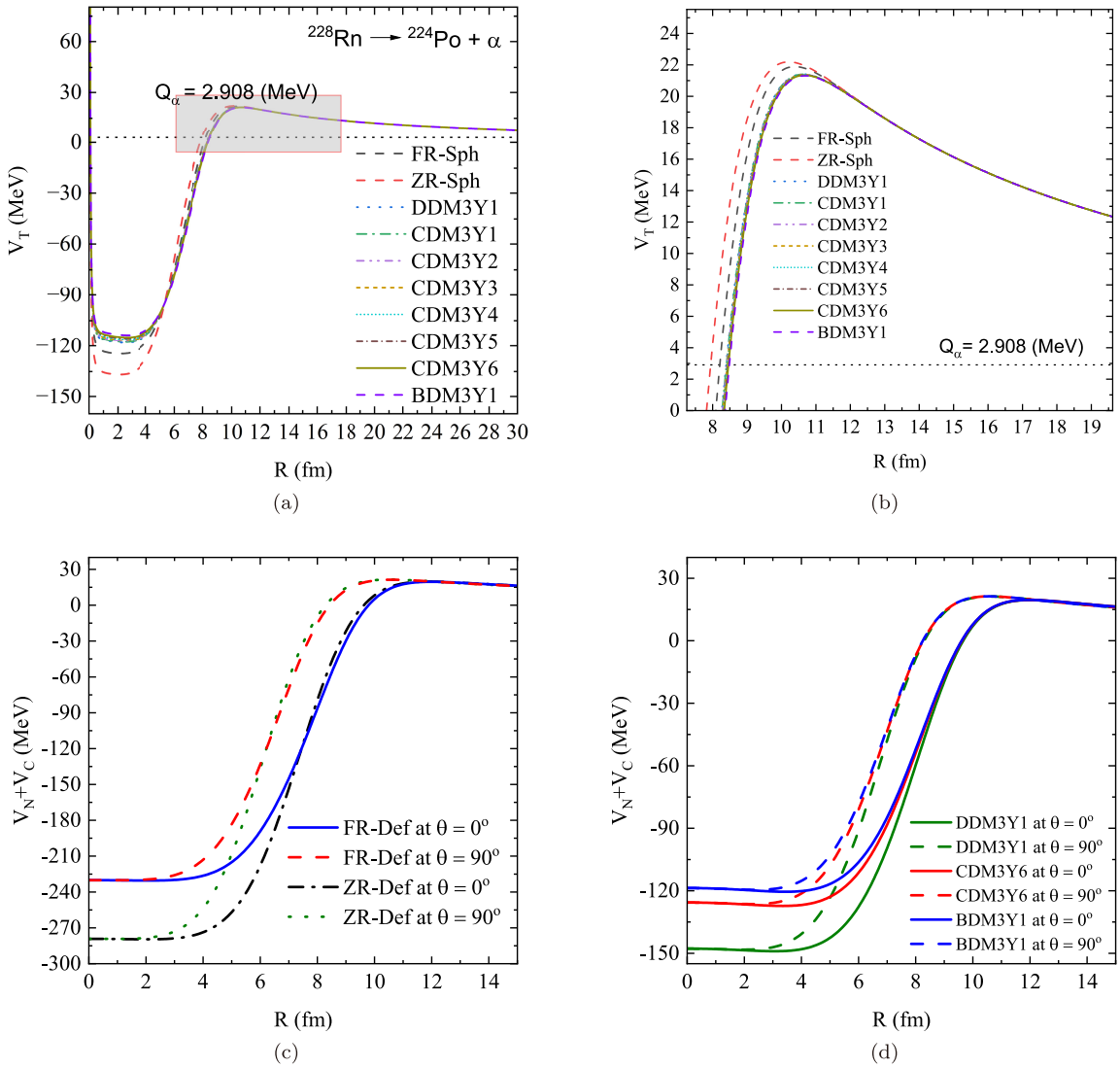


Fig. 1. (color online) The total α-nucleus interaction potential, V_T, as a function of the separation distance R for the α decay of $^{228}\mathrm{Rn} \rightarrow {}^{224}\mathrm{Po} + \alpha$, calculated using different M3Y-based effective interactions. (a) Full radial dependence of the total interaction potential, showing the nuclear pocket and the Coulomb barrier region. (b) Magnified view of the barrier region, highlighting the barrier height and position for each effective interaction. (c) Sum of the nuclear and Coulomb potentials, $V_N + V_C$, from deformed calculations using zero-range and finite-range exchange treatments at $\theta = 0°$ and 90°. (d) Sum of the nuclear and Coulomb potentials, $V_N + V_C$, from deformed density-dependent interactions, including finite-range exchange effects, at $\theta = 0°$ and 90°. The horizontal dotted line indicates the decay energy $Q_\alpha = 2.908$ MeV.

shape of the potential remains similar across all interactions, small differences emerge in the depth of the nuclear pocket and in the barrier characteristics. These variations arise from the different treatments of nuclear matter incompressibility and finite-range exchange contributions incorporated into the various M3Y-based interactions, which modify the interior part of the microscopic nuclear potential and modestly affect the barrier profile.

Figure 1(b) presents an enlarged view of the barrier region, where the quantum tunneling process responsible for α decay occurs. The horizontal dotted line represents the decay energy $Q_\alpha = 2.908$ MeV, which defines the classical turning points of the tunneling region. Although the general behavior of the potentials remains very similar, small variations in the barrier height and position are evident among the different interactions. For the reference FR-Sph interaction, the Coulomb barrier appears at $R_B \approx 10.40$ fm with a height of $V_B \approx 21.89$ MeV. When the zero-range exchange approximation (ZR-Sph) is adopted, the barrier height increases slightly to $V_B \approx 22.19$ MeV, representing an enhancement of about 1.38%, while the barrier radius shifts inward to $R_B \approx 10.20$ fm. The inclusion of density dependence in the effective interaction systematically modifies the barrier properties. In

particular, the DDM3Y1 interaction reduces the barrier height to approximately 21.41 MeV, which is about 2.2% lower than the FR-Sph result, while shifting the barrier position outward to $R_B \approx 10.65$ fm. A similar trend is observed for the CDM3Y family of interactions, where the barrier height gradually decreases from about 21.40 MeV for CDM3Y1 to 21.33 MeV for CDM3Y6, corresponding to a reduction of roughly 2.2%−2.5% relative to the FR-Sph case. Among the density-dependent models, the BDM3Y1 interaction produces the lowest barrier, $V_B \approx 21.30$ MeV at $R_B \approx 10.70$ fm, corresponding to a decrease of approximately 2.7% compared with the reference potential. These results indicate that both the density dependence and the treatment of exchange effects in the effective nucleon–nucleon interaction influence the α–nucleus potential in the vicinity of the Coulomb barrier. Although the resulting changes in the barrier height are relatively small (within a few percent), the α-decay half-life depends exponentially on the barrier penetration probability within the WKB framework. Consequently, even these modest variations in the barrier characteristics can lead to significant differences in the predicted α-decay half-lives, particularly for heavy and superheavy nuclei where the tunneling probability is extremely sensitive to the detailed shape of the interaction potential.

Figures 1(c) and 1(d) present the nuclear plus Coulomb potential, $V_N + V_C$, for deformed daughter nuclei at the two orientations $\theta = 0^\circ$ and 90°. Figure 1(c) compares the deformed calculations using zero-range and finite-range exchange treatments. The inclusion of deformation introduces a clear orientation dependence of the potential, particularly in the surface and inner-barrier regions, where the overlap between the α particle and the daughter nucleus is significant. The difference between the $\theta = 0^\circ$ and 90° curves reflects the change in the barrier width with orientation, which directly affects the WKB penetrability and, consequently, the calculated half-life.

Figure 1(d) presents the corresponding deformed density-dependent potentials for selected DDM3Y, CDM3Y, and BDM3Y interactions, including finite-range exchange effects. The potentials retain the orientation dependence induced by deformation, while the different density-dependent parametrizations produce notable changes in the depth of the inner potential and in the surface region. These differences originate from the distinct density dependences and associated nuclear incompressibility values of the effective NN interactions. In particular, the finite-range density-dependent treatment alters the barrier profile in the region relevant to tunneling, thereby affecting the calculated penetrability and half-life.

Note that all density-dependent interactions used in this work, namely DDM3Y, CDM3Y, and BDM3Y, are implemented using the finite-range exchange treatment. This choice is consistent with the construction of these density-dependent M3Y parametrizations, as their exchange components and density-dependent strengths were originally formulated and adjusted within finite-range folding calculations [33]. Therefore, applying these interactions with finite-range exchange ensures a consistent treatment of their parametrization. However, including deformation together with finite-range exchange is computationally demanding, as the exchange potential contains nonlocal density matrices and requires an iterative self-consistent determination of the local momentum for each orientation and radial point. This computational cost becomes substantial for a systematic survey of a large number of α-emitting nuclei. For this reason, the density-dependent finite-range calculations are performed within the spherical approximation in this large-scale survey, while deformation effects are examined separately using the zero-range exchange treatment.

Table 2 presents a comprehensive comparison of the calculated and experimental α-decay half-lives for 256 α emitters. Listed are the experimental decay energies $Q_\alpha^{\text{Expt.}}$, the minimum transferred angular momentum $\ell_{\min}$, and the predicted logarithmic half-lives obtained using density-dependent M3Y interactions (DDM3Y1, CDM3Y1–CDM3Y6, and BDM3Y1), alongside the corresponding experimental values. Overall, the calculated half-lives show reasonable agreement with the experimental data and reproduce the general trends across a broad range of nuclei, supporting the reliability of the microscopic double-folding approach. The strong sensitivity of the half-life to the decay energy is clearly captured; small variations in Q_α induce significant changes in $T_{1/2}$ owing to the exponential dependence of the barrier penetration probability. Furthermore, the effect of angular momentum transfer is consistently described, where nuclei requiring nonzero $\ell_{\min}$ exhibit systematically longer half-lives as a result of the centrifugal barrier.

A closer inspection of Table 2 reveals systematic differences among the various density-dependent interactions. In particular, along the CDM3Y sequence, an increase in the nuclear incompressibility parameter K is generally accompanied by a gradual decrease in the predicted α-decay half-lives. This behavior reflects the sensitivity of the tunneling probability to minor modifications in the barrier profile induced by the nuclear matter equation of state. As incompressibility increases, the resulting interaction potential slightly enhances barrier penetrability, thereby shortening the half-lives.

This trend is illustrated by specific examples from Table 2. For instance, in the decay of ^{105}Te, the predicted logarithmic half-life decreases from −6.45 with CDM3Y1 to −6.50 with CDM3Y6. This change corresponds to a reduction factor of $10^{-0.05} \approx 0.89$, representing an approximately 11% decrease in the half-life. Similarly, for ^{106}Te, the calculated values change from −4.39 to −4.44, corresponding to an approximately 11% reduction. A more pro-

Table 2. Comparison of calculated and experimental α-decay half-lives for 256 α emitters. The table presents the experimental α-decay energies $Q_\alpha^{\text{Expt.}}$ (MeV), the minimum transferred angular momentum $\ell_{\min}$, and the predicted logarithmic half-lives $\log_{10}(T_{1/2}^{\alpha}(\text{s}))$. The theoretical values are calculated using density-dependent M3Y effective nucleon–nucleon interactions (DDM3Y1, CDM3Y1–CDM3Y6, and BDM3Y1), and are compared with the corresponding experimental data.

Parent nucleus	$Q_\alpha^{\text{Expt.}}$/MeV	$\ell_{\min}$	$\log_{10}(T_{1/2}^{\alpha}/\text{s})$								
			DDM3Y1	CDM3Y1	CDM3Y2	CDM3Y3	CDM3Y4	CDM3Y5	CDM3Y6	BDM3Y1	Expt.
^{105}Te	5.069	0	−6.44	−6.45	−6.46	−6.47	−6.48	−6.49	−6.50	−6.52	−6.20
^{106}Te	4.290	0	−4.38	−4.39	−4.40	−4.41	−4.42	−4.43	−4.44	−4.46	−4.11
^{107}Te	4.010	0	−2.72	−2.73	−2.74	−2.75	−2.76	−2.78	−2.79	−2.81	−2.34
^{108}I	4.099	0	−2.77	−2.78	−2.79	−2.80	−2.81	−2.83	−2.84	−2.86	−1.58
^{109}I	3.918	2	−1.38	−1.39	−1.40	−1.41	−1.42	−1.43	−1.44	−1.47	−0.18
^{109}Xe	4.217	0	−2.68	−2.69	−2.70	−2.71	−2.72	−2.73	−2.74	−2.77	−1.89
^{110}Xe	3.872	0	−1.32	−1.33	−1.34	−1.35	−1.36	−1.38	−1.39	−1.41	−0.84
^{111}Xe	3.710	0	−0.31	−0.32	−0.33	−0.34	−0.35	−0.37	−0.38	−0.40	0.85
^{112}Xe	3.330	0	1.89	1.88	1.87	1.86	1.85	1.83	1.82	1.80	2.35
^{112}Cs	3.930	0	−0.68	−0.69	−0.70	−0.71	−0.72	−0.73	−0.75	−0.77	−0.73
^{154}Yb	5.474	0	−0.48	−0.49	−0.51	−0.52	−0.53	−0.55	−0.56	−0.59	−0.36
^{155}Lu	5.802	0	−1.04	−1.05	−1.06	−1.08	−1.09	−1.10	−1.12	−1.15	−1.12
^{156}Hf	6.026	0	−1.77	−1.78	−1.79	−1.81	−1.82	−1.84	−1.85	−1.88	−1.64
^{157}Hf	6.355	0	−2.58	−2.60	−2.61	−2.62	−2.64	−2.65	−2.67	−2.70	−0.91
^{157}Ta	6.355	5	−0.64	−0.65	−0.67	−0.68	−0.69	−0.71	−0.73	−0.76	−1.98
^{158}Ta	6.124	0	−1.18	−1.19	−1.21	−1.22	−1.23	−1.25	−1.27	−1.30	−1.31
^{159}Ta	5.681	5	1.92	1.91	1.89	1.88	1.87	1.85	1.83	1.79	0.49
^{158}W	6.613	0	−3.00	−3.01	−3.03	−3.04	−3.05	−3.07	−3.08	−3.12	−2.85
^{159}W	6.451	0	−2.19	−2.20	−2.22	−2.23	−2.24	−2.26	−2.27	−2.31	−2.09
^{160}W	6.066	0	−1.02	−1.03	−1.05	−1.06	−1.08	−1.09	−1.11	−1.14	−0.99
^{161}W	5.923	0	−0.24	−0.25	−0.27	−0.28	−0.29	−0.31	−0.33	−0.36	−0.25
^{160}Re	6.698	2	−1.83	−1.84	−1.85	−1.87	−1.88	−1.90	−1.91	−1.95	−2.26
^{161}Re	6.452	0	−1.81	−1.82	−1.83	−1.85	−1.86	−1.88	−1.89	−1.92	−1.80
^{162}Re	6.240	0	−0.68	−0.69	−0.70	−0.72	−0.73	−0.75	−0.76	−0.79	−0.94
^{163}Re	6.012	0	−0.16	−0.17	−0.19	−0.20	−0.22	−0.23	−0.25	−0.28	0.09
^{161}Os	7.069	0	−3.47	−3.48	−3.49	−3.51	−3.52	−3.54	−3.55	−3.58	−3.19
^{162}Os	6.768	0	−2.69	−2.70	−2.71	−2.73	−2.74	−2.76	−2.77	−2.81	−2.68
^{163}Os	6.673	0	−2.17	−2.18	−2.19	−2.21	−2.22	−2.24	−2.25	−2.28	−2.24
^{164}Os	6.479	0	−1.67	−1.68	−1.70	−1.71	−1.72	−1.74	−1.76	−1.79	−1.66
^{165}Os	6.335	0	−0.95	−0.96	−0.98	−0.99	−1.00	−1.02	−1.04	−1.07	−1.10
^{166}Os	6.143	0	−0.40	−0.41	−0.43	−0.44	−0.45	−0.47	−0.49	−0.52	−0.59
^{165}Ir	7.003	0	−2.85	−2.87	−2.88	−2.90	−2.91	−2.93	−2.94	−2.97	−2.57
^{166}Ir	6.722	0	−1.52	−1.53	−1.55	−1.56	−1.57	−1.59	−1.61	−1.64	−1.95
^{166}Ir	6.894	0	−2.11	−2.12	−2.14	−2.15	−2.17	−2.18	−2.20	−2.23	−1.81
^{167}Ir	6.505	0	−1.16	−1.17	−1.19	−1.20	−1.21	−1.23	−1.25	−1.28	−1.17
^{167}Ir	6.680	0	−1.76	−1.77	−1.79	−1.80	−1.81	−1.83	−1.85	−1.88	−1.50
^{168}Ir	6.381	0	−0.27	−0.29	−0.30	−0.32	−0.33	−0.35	−0.36	−0.40	−0.64
^{166}Pt	7.292	0	−3.55	−3.56	−3.58	−3.59	−3.61	−3.62	−3.64	−3.67	−3.53

Continued on next page

Table 2-continued from previous page

Parent nucleus	$Q_\alpha^{\text{Expt.}}$/MeV	$\ell_{\min}$	$\log_{10}(T_{1/2}^{\alpha}/\text{s})$								
			DDM3Y1	CDM3Y1	CDM3Y2	CDM3Y3	CDM3Y4	CDM3Y5	CDM3Y6	BDM3Y1	Expt.
^{167}Pt	7.160	0	−2.98	−2.99	−3.01	−3.02	−3.03	−3.05	−3.07	−3.10	−3.04
^{168}Pt	6.990	0	−2.58	−2.59	−2.61	−2.62	−2.63	−2.65	−2.67	−2.70	−2.70
^{169}Pt	6.858	0	−1.97	−1.98	−2.00	−2.01	−2.03	−2.05	−2.06	−2.09	−2.16
^{170}Pt	6.707	0	−1.60	−1.62	−1.63	−1.65	−1.66	−1.68	−1.69	−1.73	−1.86
^{170}Au	7.177	0	−2.18	−2.19	−2.21	−2.22	−2.23	−2.25	−2.27	−2.30	−2.58
^{170}Au	7.462	0	−3.08	−3.09	−3.11	−3.12	−3.13	−3.15	−3.17	−3.20	−2.83
^{171}Au	7.344	0	−3.14	−3.15	−3.16	−3.18	−3.19	−3.21	−3.22	−3.26	−2.76
^{172}Au	6.923	0	−1.33	−1.34	−1.36	−1.37	−1.38	−1.40	−1.42	−1.45	−1.55
^{171}Hg	7.668	2	−3.43	−3.45	−3.46	−3.48	−3.49	−3.51	−3.52	−3.56	−4.16
^{172}Hg	7.524	0	−3.46	−3.47	−3.49	−3.50	−3.51	−3.53	−3.55	−3.58	−3.64
^{173}Hg	7.378	0	−2.89	−2.90	−2.92	−2.93	−2.94	−2.96	−2.98	−3.01	−3.10
^{174}Hg	7.233	0	−2.54	−2.55	−2.57	−2.58	−2.59	−2.61	−2.63	−2.66	−2.70
^{175}Hg	7.072	0	−1.88	−1.89	−1.91	−1.92	−1.94	−1.96	−1.97	−2.01	−1.99
^{177}Tl	7.067	0	−1.50	−1.51	−1.52	−1.54	−1.55	−1.57	−1.59	−1.62	−1.61
^{177}Tl	7.874	0	−3.94	−3.95	−3.97	−3.98	−4.00	−4.01	−4.03	−4.06	−3.33
^{178}Pb	7.789	0	−3.46	−3.47	−3.49	−3.50	−3.52	−3.53	−3.55	−3.58	−3.60
^{179}Pb	7.596	2	−2.45	−2.46	−2.48	−2.49	−2.51	−2.53	−2.54	−2.58	−2.57
^{220}Th	8.973	0	−4.30	−4.31	−4.33	−4.34	−4.36	−4.37	−4.39	−4.43	−4.99
^{221}Th	8.625	2	−2.77	−2.79	−2.81	−2.82	−2.83	−2.85	−2.87	−2.91	−2.76
^{222}Th	8.133	0	−2.05	−2.06	−2.08	−2.09	−2.11	−2.13	−2.14	−2.18	−2.65
^{223}Th	7.567	2	0.42	0.41	0.39	0.38	0.36	0.34	0.32	0.29	−0.22
^{224}Th	7.299	0	0.59	0.58	0.56	0.54	0.53	0.51	0.49	0.45	0.02
^{225}Th	6.921	2	2.75	2.74	2.72	2.70	2.69	2.67	2.65	2.61	2.77
^{226}Th	6.453	0	3.81	3.80	3.78	3.76	3.75	3.72	3.71	3.67	3.27
^{227}Th	6.147	2	6.03	6.02	6.00	5.98	5.97	5.95	5.93	5.89	6.21
^{228}Th	5.520	0	8.23	8.22	8.20	8.18	8.17	8.14	8.12	8.09	7.78
^{229}Th	5.168	2	11.23	11.22	11.20	11.18	11.17	11.14	11.12	11.08	11.40
^{230}Th	4.770	0	12.73	12.71	12.69	12.68	12.66	12.64	12.62	12.58	12.38
^{232}Th	4.082	0	17.93	17.92	17.90	17.88	17.87	17.84	17.82	17.78	17.65
^{221}Pa	9.250	0	−4.49	−4.50	−4.52	−4.54	−4.55	−4.57	−4.59	−4.62	−5.23
^{223}Pa	8.340	0	−2.06	−2.07	−2.09	−2.10	−2.12	−2.14	−2.16	−2.19	−2.28
^{224}Pa	7.694	2	0.72	0.71	0.69	0.67	0.66	0.64	0.62	0.58	−0.07
^{225}Pa	7.400	2	1.42	1.40	1.38	1.37	1.35	1.33	1.31	1.28	0.23
^{226}Pa	6.987	0	2.60	2.58	2.56	2.55	2.53	2.51	2.49	2.46	2.16
^{227}Pa	6.580	0	4.11	4.09	4.07	4.06	4.04	4.02	4.00	3.96	3.43
^{228}Pa	6.265	3	6.92	6.91	6.88	6.87	6.85	6.83	6.81	6.77	6.63
^{229}Pa	5.835	1	7.78	7.76	7.74	7.73	7.71	7.69	7.67	7.63	7.44
^{230}Pa	5.439	2	10.78	10.77	10.75	10.73	10.72	10.69	10.67	10.63	10.67
^{231}Pa	5.150	0	11.41	11.39	11.37	11.36	11.34	11.32	11.30	11.26	12.01
^{222}U	9.480	0	−4.79	−4.80	−4.82	−4.84	−4.85	−4.87	−4.89	−4.92	−5.33

Continued on next page

Table 2-continued from previous page

Parent nucleus	$Q_\alpha^{\text{Expt.}}$/MeV	$\ell_{\min}$	$\log_{10}(T_{1/2}^{\alpha}/\text{s})$								
			DDM3Y1	CDM3Y1	CDM3Y2	CDM3Y3	CDM3Y4	CDM3Y5	CDM3Y6	BDM3Y1	Expt.
^{223}U	9.158	2	−3.44	−3.46	−3.47	−3.49	−3.50	−3.52	−3.54	−3.58	−4.19
^{224}U	8.628	0	−2.65	−2.67	−2.69	−2.70	−2.71	−2.73	−2.75	−2.79	−3.40
^{225}U	8.007	2	−0.19	−0.21	−0.23	−0.24	−0.26	−0.28	−0.30	−0.33	−1.21
^{226}U	7.701	0	0.10	0.08	0.07	0.05	0.04	0.02	0.00	−0.04	−0.57
^{227}U	7.235	2	2.44	2.42	2.40	2.39	2.37	2.35	2.33	2.29	1.82
^{228}U	6.800	0	3.33	3.32	3.30	3.28	3.27	3.25	3.23	3.19	2.75
^{229}U	6.476	0	5.02	5.00	4.98	4.97	4.95	4.93	4.91	4.87	4.24
^{230}U	5.993	0	6.86	6.85	6.83	6.81	6.80	6.78	6.76	6.72	6.24
^{231}U	5.576	2	9.93	9.91	9.89	9.87	9.86	9.84	9.82	9.78	9.96
^{232}U	5.414	0	9.89	9.87	9.85	9.84	9.82	9.80	9.78	9.74	9.34
^{233}U	4.909	0	13.52	13.50	13.48	13.47	13.45	13.43	13.41	13.37	12.70
^{234}U	4.858	0	13.31	13.29	13.27	13.25	13.24	13.22	13.20	13.16	12.89
^{236}U	4.573	0	15.30	15.28	15.26	15.25	15.23	15.21	15.19	15.15	14.87
^{238}U	4.270	0	17.64	17.62	17.60	17.59	17.57	17.55	17.53	17.49	17.15
^{223}Np	9.650	0	−4.75	−4.77	−4.78	−4.80	−4.81	−4.83	−4.85	−4.89	−5.60
^{224}Np	9.329	2	−3.39	−3.40	−3.42	−3.44	−3.45	−3.47	−3.49	−3.53	−4.32
^{225}Np	8.820	0	−2.65	−2.66	−2.68	−2.70	−2.71	−2.73	−2.75	−2.79	−2.19
^{226}Np	8.330	0	−1.29	−1.30	−1.32	−1.33	−1.35	−1.37	−1.39	−1.42	−1.46
^{227}Np	7.816	3	1.16	1.15	1.13	1.11	1.10	1.07	1.06	1.02	−0.29
^{228}Np	7.540	1	1.74	1.73	1.71	1.69	1.68	1.66	1.64	1.60	2.18
^{229}Np	7.020	1	3.43	3.42	3.40	3.38	3.37	3.35	3.33	3.29	2.55
^{230}Np	6.780	3	5.57	5.56	5.54	5.52	5.51	5.48	5.46	5.42	3.84
^{231}Np	6.370	1	6.18	6.16	6.14	6.12	6.11	6.09	6.07	6.03	5.17
^{233}Np	5.630	0	9.67	9.65	9.63	9.62	9.60	9.58	9.56	9.52	8.49
^{235}Np	5.194	1	12.44	12.43	12.41	12.39	12.37	12.35	12.33	12.29	12.12
^{236}Np	5.010	4	15.76	15.74	15.72	15.70	15.69	15.66	15.64	15.60	15.48
^{237}Np	4.957	1	13.98	13.97	13.95	13.93	13.91	13.89	13.87	13.83	13.83
^{229}Pu	7.600	2	1.97	1.96	1.94	1.92	1.91	1.89	1.87	1.83	2.26
^{230}Pu	7.178	0	2.79	2.77	2.75	2.74	2.72	2.70	2.68	2.64	2.02
^{231}Pu	6.839	0	4.39	4.38	4.36	4.34	4.33	4.31	4.29	4.25	3.60
^{232}Pu	6.716	0	4.60	4.58	4.56	4.55	4.53	4.51	4.49	4.45	4.03
^{233}Pu	6.420	2	6.68	6.67	6.65	6.63	6.61	6.59	6.57	6.53	6.02
^{234}Pu	6.310	0	6.35	6.34	6.32	6.30	6.29	6.27	6.25	6.21	5.72
^{235}Pu	5.951	0	8.47	8.46	8.44	8.42	8.41	8.39	8.37	8.33	7.73
^{236}Pu	5.867	0	8.49	8.48	8.46	8.44	8.42	8.40	8.38	8.34	7.96
^{238}Pu	5.593	0	9.94	9.92	9.90	9.89	9.87	9.85	9.83	9.79	9.44
^{240}Pu	5.256	0	11.88	11.87	11.85	11.83	11.81	11.79	11.77	11.73	11.32
^{241}Pu	5.140	2	13.61	13.59	13.57	13.55	13.54	13.51	13.49	13.45	13.27
^{242}Pu	4.984	0	13.60	13.58	13.56	13.54	13.53	13.50	13.48	13.44	13.07

Continued on next page

Table 2-continued from previous page

Parent nucleus	$Q_{\alpha}^{\text{Expt.}}$/MeV	$\ell_{\min}$	$\log_{10}(T_{1/2}^{\alpha}/\text{s})$								
			DDM3Y1	CDM3Y1	CDM3Y2	CDM3Y3	CDM3Y4	CDM3Y5	CDM3Y6	BDM3Y1	Expt.
^{244}Pu	4.666	0	15.80	15.78	15.76	15.74	15.73	15.70	15.68	15.64	15.41
^{229}Am	8.140	2	0.58	0.57	0.55	0.53	0.51	0.49	0.47	0.44	0.26
^{233}Am	7.060	1	4.16	4.15	4.13	4.11	4.09	4.07	4.05	4.01	3.63
^{234}Am	6.800	5	7.60	7.59	7.56	7.55	7.53	7.51	7.49	7.44	5.55
^{235}Am	6.576	1	6.19	6.18	6.16	6.14	6.12	6.10	6.08	6.04	5.19
^{236}Am	6.260	0	7.84	7.83	7.81	7.79	7.78	7.75	7.73	7.69	6.73
^{237}Am	6.200	1	7.94	7.93	7.90	7.89	7.87	7.85	7.83	7.79	7.25
^{239}Am	5.922	1	9.34	9.33	9.31	9.29	9.27	9.25	9.23	9.19	8.63
^{241}Am	5.638	1	10.88	10.87	10.85	10.83	10.81	10.79	10.77	10.73	10.14
^{243}Am	5.439	1	12.04	12.02	12.00	11.99	11.97	11.95	11.93	11.88	11.37
^{233}Cm	7.470	0	2.82	2.80	2.78	2.77	2.75	2.73	2.71	2.67	2.13
^{234}Cm	7.365	0	2.96	2.95	2.93	2.91	2.90	2.88	2.86	2.82	2.29
^{235}Cm	7.280	2	4.00	3.99	3.96	3.95	3.93	3.91	3.89	3.85	4.02
^{236}Cm	7.067	0	4.09	4.07	4.05	4.03	4.02	4.00	3.98	3.94	3.36
^{238}Cm	6.670	0	5.71	5.69	5.67	5.65	5.64	5.62	5.60	5.56	5.31
^{240}Cm	6.398	0	6.90	6.89	6.87	6.85	6.83	6.81	6.79	6.75	6.42
^{241}Cm	6.185	3	9.10	9.09	9.07	9.05	9.03	9.01	8.99	8.95	8.45
^{242}Cm	6.216	0	7.74	7.73	7.71	7.69	7.68	7.65	7.63	7.59	7.15
^{243}Cm	6.169	2	8.85	8.83	8.81	8.79	8.78	8.76	8.73	8.69	8.96
^{244}Cm	5.902	0	9.30	9.29	9.27	9.25	9.23	9.21	9.19	9.15	8.76
^{245}Cm	5.625	2	11.74	11.73	11.71	11.69	11.67	11.65	11.63	11.59	11.42
^{246}Cm	5.475	0	11.65	11.64	11.61	11.60	11.58	11.56	11.54	11.50	11.17
^{247}Cm	5.354	1	13.09	13.08	13.06	13.04	13.02	13.00	12.98	12.94	14.69
^{248}Cm	5.162	0	13.56	13.54	13.52	13.50	13.49	13.46	13.44	13.40	13.08
^{234}Bk	8.100	2	1.81	1.80	1.78	1.76	1.75	1.73	1.71	1.67	1.39
^{245}Bk	6.455	2	7.96	7.94	7.92	7.90	7.88	7.86	7.84	7.80	8.55
^{247}Bk	5.890	2	10.79	10.77	10.75	10.73	10.72	10.69	10.67	10.63	10.64
^{249}Bk	5.521	2	12.88	12.86	12.84	12.82	12.81	12.78	12.76	12.72	12.29
^{237}Cf	8.220	2	1.53	1.51	1.49	1.48	1.46	1.44	1.42	1.38	0.06
^{238}Cf	8.130	0	1.16	1.15	1.13	1.11	1.09	1.07	1.05	1.01	−0.07
^{239}Cf	7.760	0	2.62	2.61	2.59	2.57	2.56	2.54	2.52	2.48	1.63
^{240}Cf	7.711	0	2.56	2.54	2.52	2.51	2.49	2.47	2.45	2.41	1.61
^{242}Cf	7.517	0	3.24	3.22	3.20	3.19	3.17	3.15	3.13	3.09	2.54
^{243}Cf	7.420	3	4.67	4.66	4.64	4.62	4.60	4.58	4.56	4.52	2.88
^{244}Cf	7.329	0	3.92	3.91	3.89	3.87	3.86	3.83	3.81	3.77	3.19
^{245}Cf	7.259	0	4.50	4.49	4.47	4.45	4.44	4.41	4.39	4.35	3.88
^{246}Cf	6.862	0	5.78	5.77	5.75	5.73	5.71	5.69	5.67	5.63	5.11
^{247}Cf	6.503	2	8.20	8.19	8.17	8.15	8.13	8.11	8.09	8.05	7.51
^{248}Cf	6.361	0	8.01	8.00	7.98	7.96	7.94	7.92	7.90	7.86	7.46
^{249}Cf	6.293	1	8.96	8.94	8.92	8.90	8.89	8.86	8.84	8.80	10.04

Continued on next page

Table 2-continued from previous page

Parent nucleus	$Q_{\alpha}^{\text{Expt.}}$/MeV	$\ell_{\min}$	$\log_{10}(T_{1/2}^{\alpha}/\text{s})$								
			DDM3Y1	CDM3Y1	CDM3Y2	CDM3Y3	CDM3Y4	CDM3Y5	CDM3Y6	BDM3Y1	Expt.
^{250}Cf	6.129	0	9.13	9.12	9.10	9.08	9.06	9.04	9.02	8.98	8.62
^{251}Cf	6.177	5	11.04	11.03	11.00	10.99	10.97	10.94	10.92	10.88	10.45
^{252}Cf	6.217	0	8.68	8.66	8.64	8.63	8.61	8.59	8.57	8.52	7.94
^{254}Cf	5.927	0	10.15	10.13	10.11	10.09	10.08	10.05	10.03	9.99	9.23
^{240}Es	8.260	1	1.83	1.82	1.80	1.78	1.77	1.75	1.73	1.69	0.93
^{242}Es	8.160	1	2.26	2.24	2.22	2.21	2.19	2.17	2.15	2.11	1.50
^{243}Es	8.072	0	1.97	1.95	1.93	1.92	1.90	1.88	1.86	1.82	1.56
^{244}Es	7.940	1	3.11	3.10	3.08	3.06	3.04	3.02	3.00	2.96	2.87
^{246}Es	7.640	1	4.30	4.29	4.27	4.25	4.23	4.21	4.19	4.15	3.66
^{248}Es	7.160	2	6.68	6.66	6.64	6.63	6.61	6.59	6.57	6.52	5.76
^{249}Es	6.940	3	7.05	7.04	7.02	7.00	6.98	6.96	6.94	6.89	6.03
^{251}Es	6.597	0	7.78	7.77	7.74	7.73	7.71	7.69	7.67	7.62	7.38
^{252}Es	6.739	2	8.71	8.70	8.68	8.66	8.64	8.62	8.60	8.56	7.72
^{253}Es	6.739	0	7.14	7.13	7.11	7.09	7.07	7.05	7.03	6.99	6.25
^{243}Fm	8.690	1	0.60	0.59	0.57	0.55	0.53	0.51	0.49	0.45	−0.60
^{244}Fm	8.550	0	0.62	0.60	0.58	0.56	0.55	0.53	0.51	0.47	−0.46
^{245}Fm	8.440	3	1.95	1.94	1.92	1.90	1.88	1.86	1.84	1.80	0.62
^{246}Fm	8.379	0	1.13	1.12	1.10	1.08	1.06	1.04	1.02	0.98	0.22
^{247}Fm	8.258	4	2.95	2.93	2.91	2.89	2.87	2.85	2.83	2.79	1.69
^{248}Fm	7.995	0	2.37	2.36	2.34	2.32	2.30	2.28	2.26	2.22	1.54
^{250}Fm	7.557	0	3.91	3.90	3.88	3.86	3.85	3.82	3.80	3.76	3.27
^{251}Fm	7.425	1	4.94	4.93	4.91	4.89	4.87	4.85	4.83	4.79	4.25
^{252}Fm	7.154	0	5.46	5.45	5.43	5.41	5.39	5.37	5.35	5.31	4.96
^{254}Fm	7.307	0	4.84	4.82	4.80	4.78	4.77	4.74	4.72	4.68	4.07
^{256}Fm	7.025	0	5.96	5.95	5.93	5.91	5.89	5.87	5.85	5.81	5.07
^{257}Fm	6.864	2	7.52	7.50	7.48	7.46	7.45	7.42	7.40	7.36	6.94
^{244}Md	8.950	1	0.43	0.42	0.40	0.38	0.37	0.34	0.32	0.28	−0.44
^{245}Md	9.010	2	0.29	0.27	0.25	0.23	0.22	0.20	0.18	0.13	−0.42
^{246}Md	8.890	1	0.70	0.68	0.66	0.65	0.63	0.61	0.59	0.55	−0.04
^{247}Md	8.764	1	0.77	0.75	0.73	0.72	0.70	0.68	0.66	0.62	0.08
^{249}Md	8.441	2	2.02	2.01	1.99	1.97	1.95	1.93	1.91	1.87	1.53
^{250}Md	8.155	2	3.65	3.64	3.62	3.60	3.58	3.56	3.54	3.50	2.89
^{251}Md	7.963	1	3.38	3.36	3.34	3.33	3.31	3.29	3.27	3.23	3.40
^{253}Md	7.573	1	4.81	4.79	4.77	4.75	4.74	4.71	4.69	4.65	5.01
^{255}Md	7.906	2	3.84	3.83	3.80	3.79	3.77	3.75	3.73	3.68	4.36
^{256}Md	7.740	3	5.86	5.85	5.82	5.81	5.79	5.77	5.74	5.70	4.71
^{257}Md	7.557	1	4.88	4.86	4.84	4.82	4.81	4.78	4.76	4.72	5.12
^{258}Md	7.271	1	7.04	7.03	7.00	6.99	6.97	6.95	6.93	6.88	6.65
^{251}No	8.752	0	0.99	0.97	0.95	0.94	0.92	0.90	0.88	0.84	−0.02
^{252}No	8.549	0	1.37	1.35	1.33	1.31	1.30	1.28	1.26	1.21	0.56

Continued on next page

Table 2-continued from previous page

Parent nucleus	$Q_{\alpha}^{\text{Expt.}}$/MeV	$\ell_{\min}$	$\log_{10}(T_{1/2}^{\alpha}/\text{s})$								
			DDM3Y1	CDM3Y1	CDM3Y2	CDM3Y3	CDM3Y4	CDM3Y5	CDM3Y6	BDM3Y1	Expt.
^{253}No	8.415	1	2.26	2.25	2.22	2.21	2.19	2.17	2.15	2.11	2.23
^{254}No	8.226	0	2.39	2.38	2.36	2.34	2.32	2.30	2.28	2.24	1.76
^{256}No	8.582	0	1.23	1.21	1.19	1.18	1.16	1.14	1.12	1.08	0.47
^{257}No	8.477	2	2.32	2.30	2.28	2.27	2.25	2.23	2.21	2.16	1.46
^{259}No	7.854	2	4.45	4.43	4.41	4.39	4.38	4.35	4.33	4.29	3.67
^{252}Lr	9.164	0	0.36	0.34	0.32	0.31	0.29	0.27	0.25	0.21	−0.42
^{253}Lr	8.918	0	0.87	0.86	0.84	0.82	0.80	0.78	0.76	0.72	−0.15
^{254}Lr	8.822	3	2.65	2.64	2.62	2.60	2.58	2.56	2.54	2.50	1.22
^{256}Lr	8.850	1	1.85	1.84	1.81	1.80	1.78	1.76	1.74	1.70	1.52
^{255}Rf	9.055	1	1.05	1.04	1.01	1.00	0.98	0.96	0.94	0.90	0.49
^{256}Rf	8.926	0	0.98	0.97	0.95	0.93	0.92	0.89	0.87	0.83	0.33
^{257}Rf	9.083	5	2.39	2.38	2.36	2.34	2.32	2.30	2.27	2.23	0.75
^{258}Rf	9.196	0	0.18	0.16	0.14	0.13	0.11	0.09	0.07	0.03	−0.59
^{259}Rf	9.130	2	1.09	1.07	1.05	1.03	1.02	0.99	0.97	0.93	0.49
^{261}Rf	8.650	0	2.10	2.09	2.06	2.05	2.03	2.01	1.99	1.95	1.07
^{256}Db	9.340	2	1.31	1.30	1.28	1.26	1.24	1.22	1.20	1.16	0.39
^{257}Db	9.206	1	0.98	0.97	0.95	0.93	0.91	0.89	0.87	0.83	0.38
^{258}Db	9.437	5	2.59	2.58	2.56	2.54	2.52	2.50	2.47	2.43	0.53
^{259}Db	9.620	5	1.23	1.22	1.20	1.18	1.16	1.14	1.12	1.07	−0.29
^{263}Db	8.830	5	3.55	3.53	3.51	3.49	3.47	3.45	3.43	3.38	1.89
^{270}Db	8.310	0	4.54	4.53	4.51	4.49	4.47	4.45	4.43	4.39	4.67
^{259}Sg	9.765	2	0.04	0.02	0.00	−0.02	−0.03	−0.06	−0.08	−0.12	−0.40
^{260}Sg	9.901	0	−1.00	−1.01	−1.04	−1.05	−1.07	−1.09	−1.11	−1.15	−1.77
^{261}Sg	9.714	2	0.18	0.16	0.14	0.13	0.11	0.09	0.06	0.02	−0.73
^{263}Sg	9.400	0	0.61	0.59	0.57	0.55	0.54	0.51	0.49	0.45	0.03
^{265}Sg	9.050	5	3.25	3.24	3.21	3.19	3.18	3.15	3.13	3.08	1.26
^{267}Sg	8.630	0	2.96	2.94	2.92	2.90	2.88	2.86	2.84	2.80	2.80
^{269}Sg	8.580	0	3.12	3.11	3.09	3.07	3.05	3.03	3.01	2.97	2.48
^{271}Sg	8.750	0	2.58	2.57	2.54	2.53	2.51	2.49	2.46	2.42	2.50
^{260}Bh	10.400	0	−1.66	−1.67	−1.69	−1.71	−1.72	−1.75	−1.77	−1.81	−1.39
^{261}Bh	10.500	3	−1.17	−1.18	−1.21	−1.22	−1.24	−1.26	−1.28	−1.32	−1.89
^{262}Bh	10.319	0	−1.37	−1.38	−1.40	−1.42	−1.44	−1.46	−1.48	−1.52	−1.08
^{266}Bh	9.430	0	1.31	1.30	1.28	1.26	1.24	1.22	1.20	1.16	1.03
^{267}Bh	9.230	3	2.24	2.22	2.20	2.18	2.16	2.14	2.12	2.08	1.34
^{270}Bh	9.060	0	2.63	2.62	2.60	2.58	2.56	2.54	2.52	2.48	2.36
^{271}Bh	9.420	0	0.94	0.92	0.90	0.88	0.87	0.84	0.82	0.78	0.46
^{272}Bh	9.300	0	1.93	1.92	1.90	1.88	1.86	1.84	1.82	1.78	1.05
^{274}Bh	8.940	0	3.17	3.16	3.14	3.12	3.10	3.08	3.06	3.01	1.76
^{261}Hs	10.500	0	−1.58	−1.60	−1.62	−1.64	−1.65	−1.68	−1.70	−1.74	−1.89
^{263}Hs	10.730	5	−0.55	−0.57	−0.59	−0.61	−0.62	−0.65	−0.67	−0.71	−3.05

Continued on next page

Table 2-continued from previous page

Parent nucleus	$Q_\alpha^{\rm Expt.}$/MeV	$\ell_{\rm min}$	$\log_{10}(T^\alpha_{1/2}/{\rm s})$								
			DDM3Y1	CDM3Y1	CDM3Y2	CDM3Y3	CDM3Y4	CDM3Y5	CDM3Y6	BDM3Y1	Expt.
^{265}Hs	10.470	0	−1.50	−1.51	−1.53	−1.55	−1.57	−1.59	−1.61	−1.65	−2.71
^{266}Hs	10.346	0	−1.45	−1.47	−1.49	−1.51	−1.52	−1.54	−1.56	−1.61	−2.40
^{267}Hs	10.038	0	−0.40	−0.42	−0.44	−0.46	−0.47	−0.50	−0.52	−0.56	−1.16
^{268}Hs	9.760	0	0.05	0.03	0.01	−0.01	−0.02	−0.05	−0.07	−0.11	0.15
^{270}Hs	9.070	0	2.02	2.00	1.98	1.96	1.94	1.92	1.90	1.86	0.95
^{273}Hs	9.650	0	0.66	0.64	0.62	0.60	0.58	0.56	0.54	0.50	−3.62
^{275}Hs	9.450	0	1.23	1.21	1.19	1.17	1.15	1.13	1.11	1.07	−0.55
^{265}Mt	10.470	0	−1.16	−1.18	−1.20	−1.22	−1.23	−1.25	−1.28	−1.32	−2.71
^{266}Mt	10.996	0	−2.42	−2.43	−2.45	−2.47	−2.49	−2.51	−2.53	−2.57	−2.70
^{269}Mt	9.270	0	2.11	2.09	2.07	2.05	2.03	2.01	1.99	1.95	1.18
^{275}Mt	10.480	0	−1.16	−1.17	−1.19	−1.21	−1.23	−1.25	−1.27	−1.31	−1.51
^{276}Mt	10.100	0	0.30	0.28	0.26	0.24	0.23	0.20	0.18	0.14	−0.16
^{278}Mt	9.580	0	1.90	1.89	1.87	1.85	1.83	1.81	1.79	1.74	0.78
^{267}Ds	11.780	0	−3.78	−3.79	−3.81	−3.83	−3.85	−3.87	−3.89	−3.93	−5.00
^{269}Ds	11.510	0	−3.21	−3.22	−3.24	−3.26	−3.28	−3.30	−3.32	−3.36	−3.64
^{270}Ds	11.117	0	−2.61	−2.62	−2.64	−2.66	−2.68	−2.70	−2.72	−2.76	−3.69
^{271}Ds	10.870	0	−1.77	−1.79	−1.81	−1.82	−1.84	−1.86	−1.88	−1.93	−0.24
^{273}Ds	11.370	0	−2.89	−2.91	−2.93	−2.95	−2.96	−2.98	−3.01	−3.05	−3.62
^{282}Ds	9.150	0	2.46	2.44	2.42	2.40	2.38	2.36	2.34	2.29	2.40

nounced effect is observed for heavier nuclei; for example, in ^{161}W, the predicted logarithmic half-life decreases from −0.25 with CDM3Y1 to −0.33 with CDM3Y6, corresponding to a factor of $10^{-0.08} \approx 0.83$, or nearly a 17% reduction. These examples demonstrate that even minor variations in $\log_{10}(T_{1/2})$ translate into non-negligible differences in the half-lives.

The BDM3Y1 interaction often yields even shorter half-lives, tending to provide predictions closer to the experimental values for many nuclei; this suggests an improved balance between nuclear attraction and Coulomb repulsion through its specific density dependence. For example, for ^{105}Te, the logarithmic half-life obtained with BDM3Y1 is −6.52, compared with −6.45 for CDM3Y1, corresponding to a reduction factor of $10^{-0.07} \approx 0.85$, or approximately 15%.

We computed the standard deviation σ of the decimal logarithmic deviations between the calculated and experimental half-lives

$$\sigma = \left[\frac{1}{n-1}\sum_{i}^{n}(\log_{10}T_{1/2}^{\rm Calc.} - \log_{10}T_{1/2}^{\rm Expt.})^2\right]^{1/2}. \quad (37)$$

To quantify the global agreement between theory and experiment, the standard deviation σ of the logarithmic differences is calculated according to Eq. (37), with the results summarized in Table 3. The statistical analysis confirms the trends observed in Table 2. The density-independent interactions exhibit reasonable agreement,

Table 3. The standard deviation σ for the considered M3Y-Paris interactions. The incompressibility K is listed exclusively for density-dependent variants.

Interaction	K/MeV	σ
Density-independent M3Y-Paris interactions		
FR-Sph	—	1.066
ZR-Sph	—	1.414
ZR-Def	—	1.084
Density-dependent M3Y-Paris interactions		
DDM3Y1	176	0.819
CDM3Y1	188	0.811
CDM3Y2	204	0.798
CDM3Y3	217	0.788
CDM3Y4	228	0.779
CDM3Y5	241	0.766
CDM3Y6	252	0.756
BDM3Y1	270	0.734

with FR-Sph and ZR-Def yielding $\sigma = 1.066$ and 1.084, respectively, while the ZR-Sph interaction shows a significantly larger deviation ($\sigma = 1.414$), indicating greater dispersion. In contrast, the inclusion of density dependence leads to a systematic improvement. The standard deviation decreases progressively along the CDM3Y series from 0.811 to 0.756 as the incompressibility parameter increases, while the BDM3Y1 interaction provides the best overall agreement, yielding $\sigma = 0.734$. This reduction in σ clearly demonstrates the importance of incorporating density dependence into the effective nucleon–nucleon interaction.

The global behavior of these deviations is further illustrated in Fig. 2, where $\log_{10}(T^{\rm calc}_{1/2}/T^{\rm exp}_{1/2})$ is plotted as a function of the parent proton number Z_p. Consistent with the statistical results, the density-dependent interactions exhibit a more compact distribution of data points around zero, with most values lying within ±2 orders of magnitude. In contrast, the density-independent interactions display greater scatter, particularly for heavy and superheavy nuclei. These observations indicate that the inclusion of density dependence, together with nuclear incompressibility and exchange effects, improves the overall description of α-decay half-lives within the present global calculation. Although the variations in the interaction potential are relatively small, their impact on the tunneling probability is amplified by the exponential nature of the WKB formalism, leading to appreciable differences in the predicted decay properties.

However, deviations outside the interval $-2 \le \Delta \le 2$, where $\Delta = \log_{10}(T^{\rm calc}_{1/2}/T^{\rm exp}_{1/2})$, represent discrepancies exceeding two orders of magnitude. Therefore, such cases should not be interpreted as precise quantitative agreement. The present comparison is intended as a large-scale systematic test of the adopted microscopic α–daughter potentials rather than a refitting of the decay-model parameters for individual nuclei. The calculations employ consistent input prescriptions throughout the dataset, including the adopted Q_α values and the α-particle preformation probabilities obtained from the analytical formula of Deng and Zhang [64], without additional parameter fitting. Consequently, the deviations shown in Fig. 2 reflect not only the sensitivity to the effective NN interaction and exchange treatment but also uncertainties associated with Q_α values, global preformation parametrization, angular-momentum assignments, and deformation treatment. The larger deviations observed for some nuclei, especially in the region $90 \le Z_p \le 110$, suggest that refined local inputs—such as improved Q_α values, nucleus-dependent preformation factors, or more detailed deformation effects—may be required to achieve accurate quantitative descriptions.

Figures 3 and 4 present a detailed comparison of calculated and experimental logarithmic α-decay half-lives, $\log_{10} T_{1/2}$, plotted as a function of the daughter nucleus neutron number, N_d, for several isotopic chains ranging from medium-mass to superheavy nuclei. These figures provide valuable insight into the evolution of α-decay properties along isotopic chains and, in particular, highlight the influence of neutron shell closures on decay behavior.

In Fig. 3, which includes Te ($Z_p = 52$), Hf ($Z_p = 72$), W ($Z_p = 74$), and Po ($Z_p = 84$) isotopes, the calculated results obtained using various M3Y-based interactions

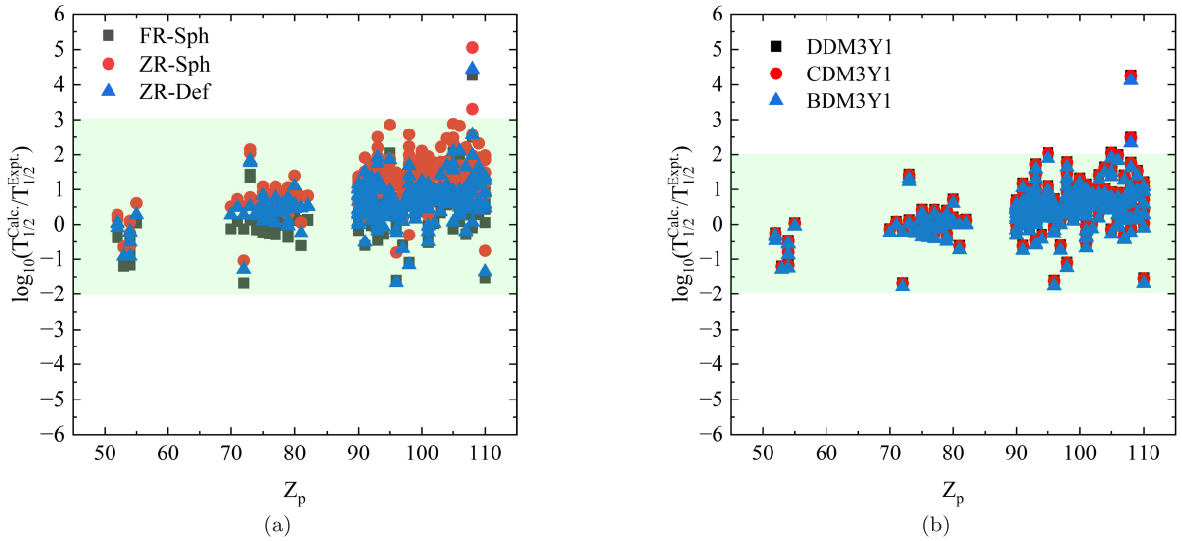


Fig. 2. (color online) Deviations between the calculated and experimental α-decay half-lives, $\log_{10}(T^{\rm Calc}_{1/2}/T^{\rm Expt}_{1/2})$, are plotted as a function of the atomic number of the parent nucleus, Z_p. The predictions are obtained using various M3Y-based effective interactions. Panel (a) shows the results for the FR-Sph, ZR-Sph, and ZR-Def interactions, while panel (b) presents those for the density-dependent interactions DDM3Y1, CDM3Y1, and BDM3Y1. The shaded region indicates deviations within ±2 orders of magnitude of the experimental half-lives.

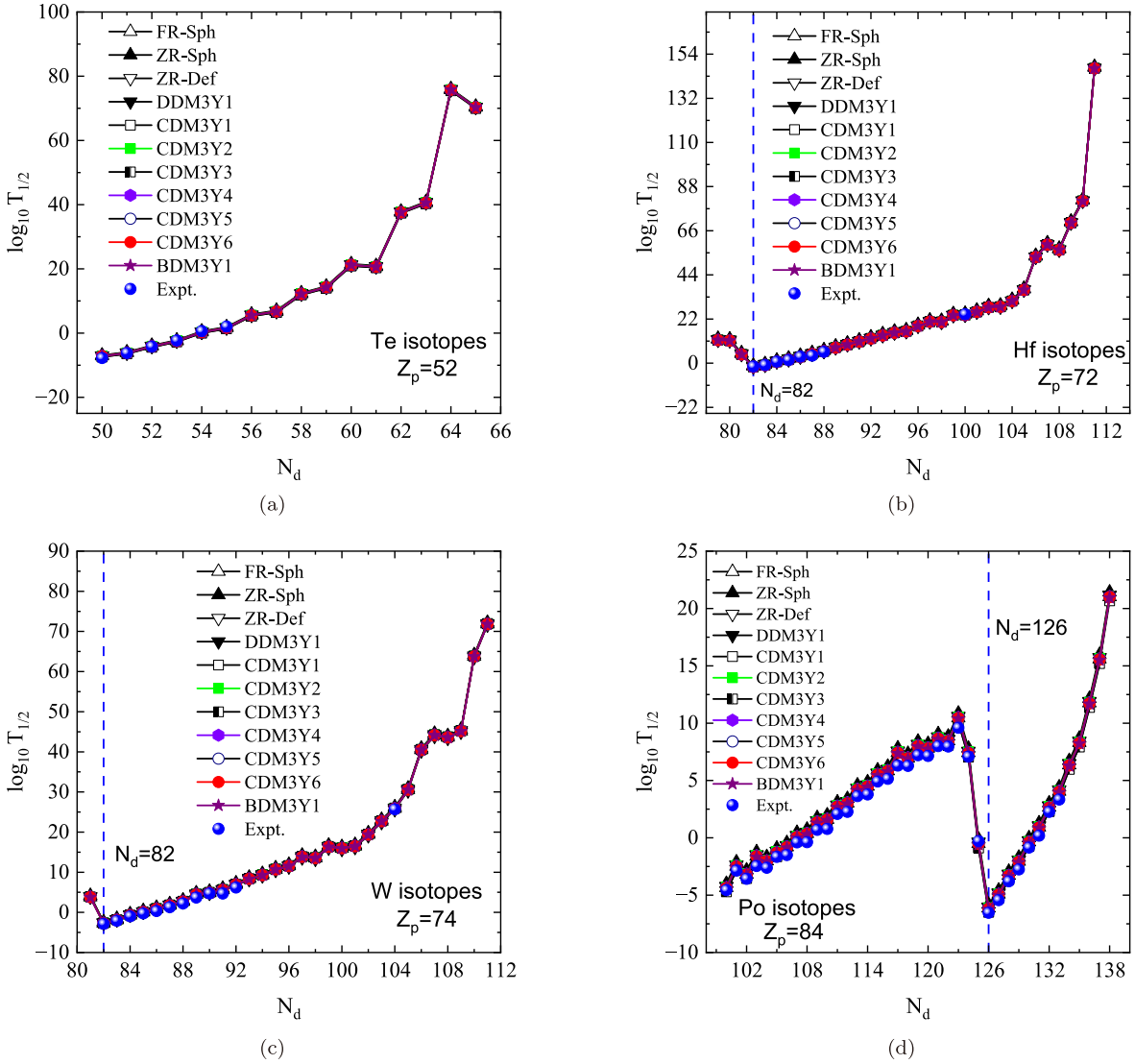


Fig. 3. (color online) The calculated and experimental logarithmic α-decay half-lives, $\log_{10} T_{1/2}$ (s), are plotted as a function of the neutron number of the daughter nucleus, N_d, for several isotopic chains. The theoretical results are obtained using different M3Y-based effective interactions. The panels correspond to (a) Te isotopes ($Z_p = 52$), (b) Hf isotopes ($Z_p = 72$), (c) W isotopes ($Z_p = 74$), and (d) Po isotopes ($Z_p = 84$). The vertical dashed lines indicate the neutron shell closures at $N_d = 82$ and $N_d = 126$, highlighting the influence of shell effects on the α-decay half-lives. Experimental data are shown for comparison.

closely follow the experimental data over the entire range of neutron numbers. A general increase in $\log_{10} T_{1/2}$ with N_d is observed, reflecting the gradual reduction in Q_α values and the corresponding decrease in tunneling probability. However, superimposed on this smooth trend, clear irregularities emerge in the vicinity of the neutron magic number $N_d = 82$, as indicated by the vertical dashed lines. Around this shell closure, a noticeable change in slope and, in some cases, local enhancements of the half-lives are observed. This behavior can be attributed to the increased stability associated with closed neutron shells, which leads to reduced decay energies and, consequently, longer half-lives.

A similar effect is evident in the Po isotopic chain, where an additional pronounced structure emerges near the neutron shell closure at $N_d = 126$. In this region, the half-lives exhibit sharp variations, including a distinct minimum followed by a rapid increase. This characteristic behavior reflects the interplay between shell effects and pairing correlations, as well as the sudden change in nuclear structure upon crossing a magic number. The ability of the theoretical model to reproduce these features indicates that the microscopic potentials derived from the M3Y interactions effectively incorporate the essential physics governing shell effects in α decay.

Figure 4 extends this analysis to superheavy nuclei, including the Lv ($Z_p = 116$), Og ($Z_p = 118$), $Z_p = 120$, and $Z_p = 122$ isotopic chains. In these systems, the influence

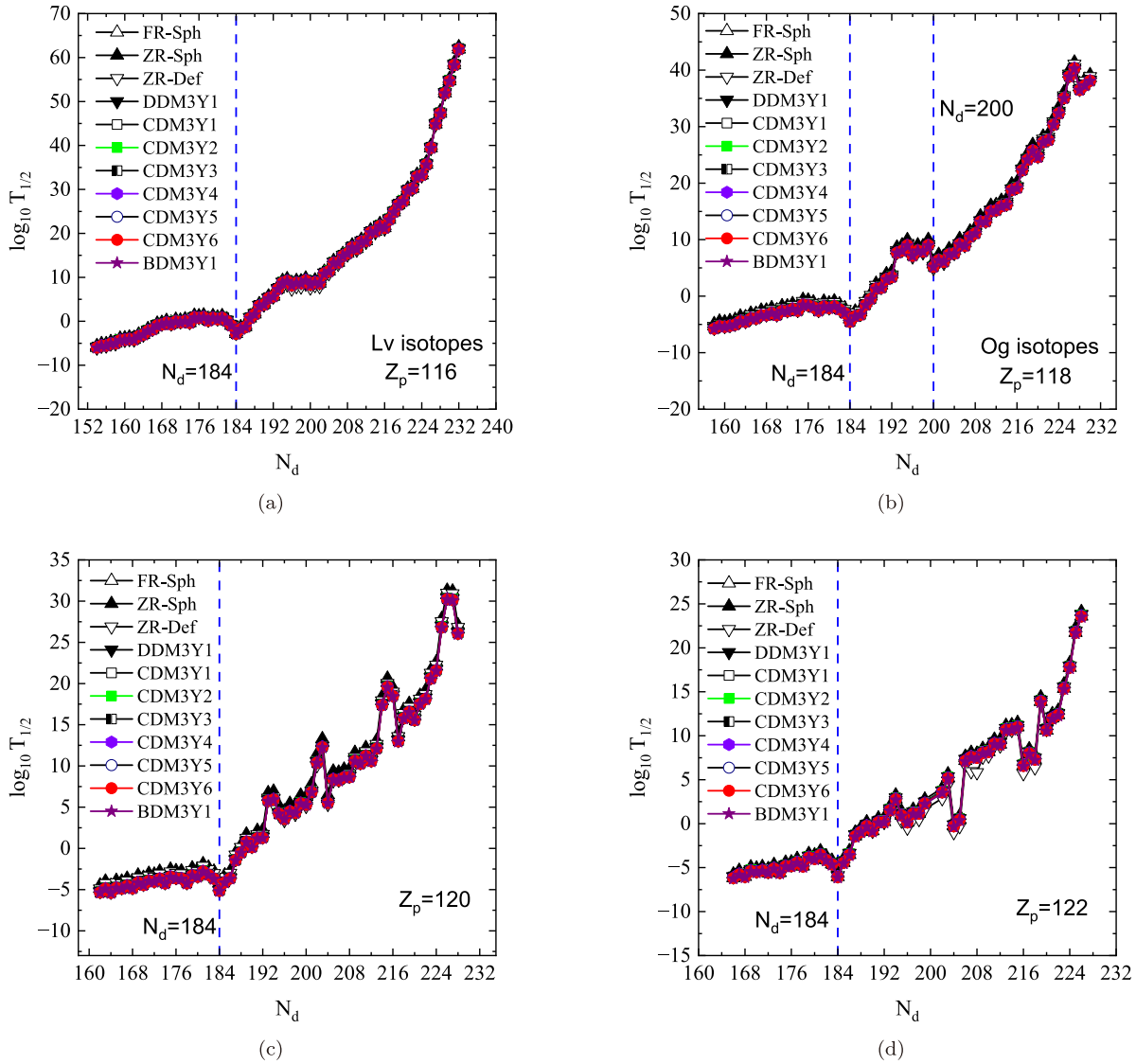


Fig. 4. (color online) Same as Fig. 3, but for superheavy isotopic chains: (a) Lv isotopes ($Z_p = 116$), (b) Og isotopes ($Z_p = 118$), (c) $Z_p = 120$ isotopes, and (d) $Z_p = 122$ isotopes. The vertical dashed lines denote the neutron shell closures at $N_d = 184$ and $N_d = 200$.

of shell closures becomes even more pronounced due to the delicate balance between strong Coulomb repulsion and shell stabilization effects. The vertical dashed lines indicate the predicted neutron shell closures at $N_d = 184$ and $N_d = 200$. Around $N_d = 184$, a clear change in the half-life trend is observed across all isotopic chains, often manifested as a local increase or kink in $\log_{10} T_{1/2}$. This behavior is consistent with the enhanced stability expected for the next major neutron magic number in the superheavy region.

Beyond $N_d = 184$, the half-lives generally increase more rapidly with neutron number, reflecting decreasing Q_α values and the growing influence of the Coulomb barrier. In some cases, additional irregularities appear near $N_d = 200$, suggesting the possible presence of a subshell or emerging shell structure in this region. The abrupt changes observed for the $Z_p = 120$ and $Z_p = 122$ chains after $N_d = 192$ are mainly driven by local variations in the adopted Q_α values. This is expected because the WKB penetrability depends exponentially on the barrier action and is therefore highly sensitive to the decay energy. For example, in the $Z_p = 120$ chain, the decrease in Q_α from 9.100 MeV at $N_d = 201$ to 7.699 MeV at $N_d = 203$ leads to a pronounced increase in the calculated half-life, while the subsequent increase in Q_α to 9.273 MeV at $N_d = 204$ produces a sharp reduction in $\log_{10} T_{1/2}$. Similar behavior is observed for the $Z_p = 122$ chain, where local variations in Q_α around N_d =203−206 generate sharp changes in the calculated half-lives. Although deformation modifies the barrier profile and generally reduces the calculated half-lives, its isotopic variation is smoother than the local changes induced by the Q_α systematics. Therefore, de-

formation affects the overall magnitude of the half-life systematics, whereas the abrupt structures in this region are more directly connected to Q_α-driven tunneling sensitivity, which may reflect local shell or subshell features on the mass surface. Although experimental data for superheavy nuclei remain limited, the theoretical predictions exhibit broadly consistent trends across the different interactions, supporting the reliability of the present systematic comparison.

Overall, Figs. 3 and 4 demonstrate that the microscopic double-folding approach based on M3Y-type interactions effectively describes the general systematics of α-decay half-lives and their sensitivity to neutron shell closures. The observed kinks, slope changes, and local extrema around magic neutron numbers indicate the influence of shell effects on the stability and decay properties of both medium-mass and superheavy nuclei. It should be noted, however, that the present analysis primarily examines the sensitivity of the calculated half-lives to the microscopic interaction, density dependence, deformation, and exchange treatment, whereas the adopted Q_α values and α-particle preformation probabilities serve as external inputs. These inputs also influence the absolute half-life predictions and must be considered when interpreting the quantitative agreement with experiment. Therefore, a quantitative description of α decay requires a realistic treatment of the nuclear interaction, including density dependence and its connection to nuclear matter properties, together with reliable decay-energy and preformation inputs.

IV. SUMMARY AND CONCLUSION

In this work, the α-decay half-lives of nuclei in the range $52 \le Z \le 122$ have been systematically investigated within a microscopic double-folding framework using the M3Y-Paris effective nucleon–nucleon interaction and its density-dependent extensions, namely, DDM3Y, CDM3Y, and BDM3Y. The calculated α-nucleus potentials exhibit the characteristic structure of an attractive nuclear pocket followed by a repulsive Coulomb barrier, where the detailed barrier properties depend on the treatment of exchange effects and density dependence. Owing to the exponential sensitivity of the WKB tunneling probability, even small variations in the barrier height and position lead to noticeable changes in the predicted α-decay half-lives. A systematic comparison with experimental data for 256 α emitters demonstrates that the microscopic approach reproduces the overall α-decay systematics across medium-mass, heavy, and superheavy nuclei, although certain nuclei still require refined local inputs to achieve improved quantitative agreement.

The results indicate a clear sensitivity of the calculated half-lives to the nuclear incompressibility incorporated into the density-dependent interaction. Increasing the incompressibility parameter K within the CDM3Y family reduces the predicted α-decay half-lives, reflecting a slight enhancement in barrier penetrability. This trend is supported by both comparisons of individual isotopes and global statistical analysis, which shows a progressive decrease in the standard deviation with increasing K. Among the considered interactions, BDM3Y1 yields the smallest global deviation from the experimental data. Furthermore, the calculated isotopic trends reflect distinct variations around neutron shell closures at $N_d = 82$, 126, and 184, underscoring the interplay between nuclear structure effects and barrier penetration. These results demonstrate that nuclear incompressibility, density dependence, deformation, and exchange effects are crucial factors in determining α-decay half-lives within the microscopic double-folding approach.

References

[1] W. M. Seif, G. G. Adamian, N. V. Antonenko *et al.*, Phys. Rev. C **104**, 014317 (2021)
[2] M. Ismail and A. Adel, Phys. Rev. C **97**, 044301 (2018)
[3] M. Ismail, A. Y. Ellithi, A. Adel *et al.*, Phys. Scr. **97**, 075303 (2022)
[4] A. Adel and A. R. Abdulghany, Phys. Scr. **96**, 125314 (2021)
[5] W. Ye, Y. Qian, and Z. Ren, Phys. Rev. C **104**, 064308 (2021)
[6] K. P. Santhosh, C. Nithya, H. Hassanabadi *et al.*, Phys. Rev. C **98**, 024625 (2018)
[7] X. J. Bao, S. Q. Guo, H. F. Zhang *et al.*, J. Phys. G: Nucl. Part. Phys. **42**, 085101 (2015)
[8] M. Ismail, A. Adel, A. Y. Ellithi *et al.*, Sci. Rep. **16**, 5304 (2026)
[9] M. Ismail, A. Adel, A. Y. Ellithi *et al.*, Phys. Scr. **100**, 125309 (2025)
[10] Y. Oganessian, J. Phys. G: Nucl. Part. Phys. **34**, R165 (2007)
[11] J. H. Hamilton, S. Hofmann, and Y. T. Oganessian, Annu. Rev. Nucl. Part. Sci. **63**, 383 (2013)
[12] Y. T. Oganessian and V. K. Utyonkov, Rep. Prog. Phys. **78**, 036301 (2015)
[13] Y. T. Oganessian and V. K. Utyonkov, Nucl. Phys. A **944**, 62 (2015)
[14] Y. T. Oganessian and K. P. Rykaczewski, Phys. Today **68**, 32 (2015)
[15] Y. T. Oganessian, A. Sobiczewski, and G. M. Ter-Akopian, Phys. Scr. **92**, 023003 (2017)
[16] Y. T. Oganessian, V. K. Utyonkov, Y. V. Lobanov *et al.*, Phys. Rev. C **74**, 044602 (2006)
[17] N. T. Brewer, V. K. Utyonkov, K. P. Rykaczewski *et al.*, Phys. Rev. C **98**, 024317 (2018)
[18] M. Ismail and A. Adel, Phys. Rev. C **101**, 024607 (2020)
[19] D. Ni and Z. Ren, Phys. Rev. C **81**, 024315 (2010)
[20] C. Xu and Z. Ren, Phys. Rev. C **73**, 041301 (2006)

[21] C. Xu and Z. Ren, Nucl. Phys. A **753**, 174 (2005)
[22] M. Ismail, A. Y. Ellithi, M. M. Botros *et al*., Phys. Rev. C **81**, 024602 (2010)
[23] M. Ismail, A. Adel, A. Y. Ellithi *et al*., Chin. J. Phys. **92**, 1097 (2024)
[24] N. G. Kelkar and H. M. Castañeda, Phys. Rev. C **76**, 064605 (2007)
[25] J. E. Perez Velasquez, N. G. Kelkar, and N. J. Upadhyay, Phys. Rev. C **99**, 024308 (2019)
[26] D. F. Rojas-Gamboa, J. E. P. Velasquez, N. G. Kelkar *et al*., Phys. Rev. C **105**, 034311 (2022)
[27] D. T. Khoa, Phys. Rev. C **63**, 034007 (2001)
[28] A. Adel and T. Alharbi, Braz. J. Phys. **50**, 454 (2020)
[29] M. Ismail and A. Adel, J. Phys. G: Nucl. Part. Phys. **46**, 075105 (2019)
[30] A. Adel and T. Alharbi, Nucl. Phys. A **975**, 1 (2018)
[31] A. Adel and T. Alharbi, Phys. Rev. C **92**, 014619 (2015)
[32] M. Ismail and A. Adel, Phys. Rev. C **89**, 034617 (2014)
[33] D. T. Khoa, G. R. Satchler, and W. von Oertzen, Phys. Rev. C **56**, 954 (1997)
[34] W. M. Seif, J. Phys. G: Nucl. Part. Phys. **38**, 035102 (2011)
[35] K. Chatziioannou, H. T. Cromartie, S. Gandolfi *et al*., Rev. Mod. Phys. **97**, 045007 (2025)
[36] J. P. Blaizot, Phys. Rep. **64**, 171 (1980)
[37] W. M. Seif, Phys. Rev. C **74**, 034302 (2006)
[38] S. Shlomo, V. M. Kolomietz, and G. Colò, Eur. Phys. J. A **30**, 23 (2006)
[39] M. Karakoç, F. Koyuncu, and O. Bayrak, Braz. J. Phys. **56**, 68 (2026)
[40] B. Cochet, K. Bennaceur, J. Meyer *et al*., Int. J. Mod. Phys. E **13**, 187 (2004)
[41] D. T. Khoa, W. von Oertzen, and H. G. Bohlen, Phys. Rev. C **49**, 1652 (1994)
[42] G. R. Satchler and W. G. Love, Phys. Rep. **55**, 183 (1979)
[43] H. Zhang, W. Zuo, J. Li *et al*., Phys. Rev. C **74**, 017304 (2006)
[44] G. Royer and R. Moustabchir, Nucl. Phys. A **683**, 182 (2001)
[45] C. Xu and Z. Ren, Phys. Rev. C **74**, 014304 (2006)
[46] C. Xu and Z. Ren, Nucl. Phys. A **760**, 303 (2005)
[47] K. P. Santhosh and C. Nithya, At. Data Nucl. Data Tables **119**, 33 (2018)
[48] K. Santhosh and B. Priyanka, Nucl. Phys. A **940**, 21 (2015)
[49] K. Santhosh, S. Sahadevan, and J. G. Joseph, Nucl. Phys. A **850**, 34 (2011)
[50] X.-D. Sun, J.-G. Deng, D. Xiang *et al*., Phys. Rev. C **95**, 044303 (2017)
[51] X.-D. Sun, P. Guo, and X.-H. Li, Phys. Rev. C **93**, 034316 (2016)
[52] M. Ismail, A. Adel, and A. Ibrahim, Chin. Phys. C **49**, 034106 (2025)
[53] V. Y. Denisov, Phys. Rev. C **110**, 014604 (2024)
[54] G. Saxena, P. K. Sharma, and P. Saxena, J. Phys. G: Nucl. Part. Phys. **48**, 055103 (2021)
[55] G. Royer, Nucl. Phys. A **848**, 279 (2010)
[56] M. Ismail, W. M. Seif, A. Adel *et al*., Nucl. Phys. A **958**, 202 (2017)
[57] R. E. Langer, Phys. Rev. **51**, 669 (1937)
[58] N. Wang, M. Liu, X. Wu *et al*., Phys. Lett. B **734**, 215 (2014)
[59] B. Buck, J. C. Johnston, A. C. Merchant *et al*., Phys. Rev. C **53**, 2841 (1996)
[60] M. Wang, W. J. Huang, F. G. Kondev *et al*., Chin. Phys. C **45**, 030003 (2021)
[61] N. Wang and M. Liu, Phys. Rev. C **84**, 051303 (2011)
[62] J.-G. Deng and H.-F. Zhang, Phys. Rev. C **102**, 044314 (2020)
[63] G. Royer, J. Phys. G: Nucl. Part. Phys. **26**, 1149 (2000)
[64] J.-G. Deng, H.-F. Zhang, and G. Royer, Phys. Rev. C **101**, 034307 (2020)
[65] C. Qi, F. R. Xu, R. J. Liotta *et al*., Phys. Rev. Lett. **103**, 072501 (2009)
[66] M. J. Rhoades-Brown, V. E. Oberacker, M. Seiwert *et al*., Z. Phys. A **310**, 287 (1983)
[67] B. Sinha, Phys. Rep. **20**, 1 (1975)
[68] X. Campi and A. Bouyssy, Phys. Lett. B **73**, 263 (1978)
[69] M. Ismail, M. M. Osman, and F. Salah, Phys. Rev. C **60**, 037603 (1999)
[70] W. A. Yahya, J. T. Majekodunmi, S. I. B. van der Ventel *et al*., Phys. Rev. C **111**, 024322 (2025)